Abundance Matching with the Galaxies of the Virgo Cluster and the Stellar-to-Halo Mass Relation

by

Jonathan Grossauer

A thesis
presented to the University of Waterloo
in fulfillment of the
thesis requirement for the degree of
Master of Science
in
Physics

Waterloo, Ontario, Canada, 2012

I hereby declare that I am the sole author of this thesis. This is a true copy of the thesis, including any required final revisions, as accepted by my examiners.

I understand that my thesis may be made electronically available to the public.

Abstract

Using data from the Next Generation Virgo Cluster Survey and high-resolution simulations of Virgo cluster-like halos, we determine the stellar-to-halo mass relation (SHMR) for subhalos, using the technique of abundance matching. The subhalo SHMR differs markedly from its field galaxy counterpart, regardless of how the subhalo mass is defined (mass at $z = 0$, mass at infall, or maximum mass while in the field). The slope of the relation at low mass ($M_\star < 10^{10}\,\mathrm{M}_\odot$) is in all cases steeper than the same for the field. We find conflicting indicators of whether this difference in slope indicates an increasing or decreasing dark-to-stellar ratio; further modelling is required to reach a definitive conclusion. We also find evidence for the existence of a measurable age gradient in velocity, such that older subhalos have lower velocities than their younger peers. This opens the possibility that good quality redshifts of the lower mass galaxies of the Virgo cluster might provide additional constraints on the SHMR at high redshift and its evolution. Finally, we investigate the degree to which mergers, particularly major mergers, cause mixing of old and new material in halos, which has implications for the robustness of any implied radial age gradient. We find only a slight increase in mixing for major mergers over minor mergers, and little evidence for any large amount of mixing being induced by mergers of any ratio.

Acknowledgements

I would like to thank my supervisor, James Taylor, for his direction and assistance, my friends and family for their support, and everyone else who aided me in this endeavour and made it possible.

Table of Contents

Chapter 1

Introduction

In this chapter, we provide the necessary background to understand this work. We first present an overview of cosmology and dark matter halos, and then the more specific topic of the relation between dark matter and galaxies in order to put this work into context.

1.1 Cosmology

According to the currently generally accepted, observationally-based "concordance" model of cosmology, the ΛCDM (cosmological constant Λ plus Cold Dark Matter) model , the universe we live in is expanding, flat, homogeneous and isotropic on large scales, and contains three major components: baryonic matter, cold dark matter, and a cosmological constant.

1.1.1 An Expanding, Flat Universe

The universe is expanding. The distance between two points otherwise at rest increases with time. This expansion was first observed by Hubble, who noted that the velocity at which galaxies are receding from us, measured through the redshifting of their light, was dependent on their distance. At small distances, this relation is linear:

$$v = H_0 d \tag{1.1}$$

The value H_0 is the *Hubble constant*, with a value around $70\,\mathrm{km\,s^{-1}\,Mpc^{-1}}$. It is often expressed through the quantity h, defined as $H_0 = h \cdot 100\,\mathrm{km\,s^{-1}\,Mpc^{-1}}$. In practice, the measured redshift of an object comes from two sources: the expansion of the universe, and the motion relative to this, called the *peculiar velocity*.

Modulo these peculiar velocities, redshift can thus be used as a measure of distance. However, the further the distance to an object, the longer light emitted by it has taken to reach us. Thus, redshift is also a measure of time. A galaxy with a measured redshift of $z = 1$ is both 2.4 Gpc away and viewed at a time when the universe was 7.7 Gyr younger.

The coordinate system in which two points at rest relative to each other except for the expansion of the universe is called *comoving coordinates*. The relationship between comoving and proper distance is $d_{proper} = a d_{comoving}$. The proportionality factor a is referred to as the *scale factor*, and is normalized 1 at the present day. The redshift and scale factor are directly related: $z + 1 = a^{-1}$. Thus, a galaxy with a measured redshift of $z = 1$ is viewed at a time when the universe was a factor of 2 smaller.

By a flat universe, it is meant that spacetime has zero global curvature: parallel lines remain at a constant separation as they are extended. This is in contrast to an open universe, which has negative curvature and divergent parallel lines, and a closed universe, which has positive curvature and convergent parallel lines. In order for the universe to be flat, the average mass density of the universe must be equal to the critical density,

$$\rho_c = \frac{3{H_0}^2}{8\pi G} \tag{1.2}$$

It is useful to measure mass densities relative to the critical density. Such quantities are denoted with the symbol Ω, e.g. $\Omega_{m,0}$, the density of matter at the present day.

The homogeneity and isotropy of the universe means that, on large ($\sim 100\,\mathrm{Mpc}$) scales, the universe looks the same in all directions and at any point.

1.1.2 The Components of the Universe

The first component of the universe is baryonic matter. This is the ordinary, everyday matter, protons and neutrons, which makes up planets, stars, and everything else that can

be directly observed. Only a minority of this matter is in the form of stars; the majority consists of gas in and between galaxies.

However, while baryonic matter is the most obvious component of the universe, it is only a small fraction of the total matter density, less than 20 %. The dominant form of matter in the universe is *dark matter*. This as-yet-undetermined form of matter interacts only weakly, through the weak force and gravity. As it does not interact through the electromagnetic force, unlike baryonic matter, it is invisible to direct observation. It can only be observed through its gravitational effects. In the ΛCDM, this matter is cold, meaning the particles of which it consists have been non-relativistic, traveling much slower than the speed of light, since early in the universe's history.

Matter of both sorts, taken together, still comprises only a minority of the total mass-energy density of the universe: $\Omega_{b,0} = 0.045$, $\Omega_{CDM,0} = 0.226$ (Komatsu et al., 2011). The remainder consists of the even more mysterious *dark energy*. Since near the end of the twentieth century, observations, beginning with those of distant supernovae, have indicated that the expansion of the universe is accelerating. This requires an additional hidden component with negative pressure, the repulsion from which counteracts the decelerating effect of matter on the expansion. In the ΛCDM model, this takes the form of a cosmological constant, with constant density.

There is additionally a radiation component and a relativistic neutrino component to the universe; however, these are very minor, and have negligible effect on the current evolution of the universe.

1.1.3 The Case for Dark Matter

The first evidence for dark matter came from Fritz Zwicky in the 1930's. Observing the galaxies of the Coma cluster, he noted that the galaxies were moving much too fast to be gravitationally bound by the visible matter alone. In order to hold the cluster together, there would have had to be 20 times more mass than what was inferred from visible light. He posited that this missing mass was in the form of "dark matter" invisible to observation.

Zwicky's idea of a dark matter was ignored, however, until the 1970's, when Vera Rubin made observations of galaxy rotation curves. The stars and gas in a spiral galaxy orbit the center of the galaxy in a thin disk. This disk is not in rigid rotation: each star and

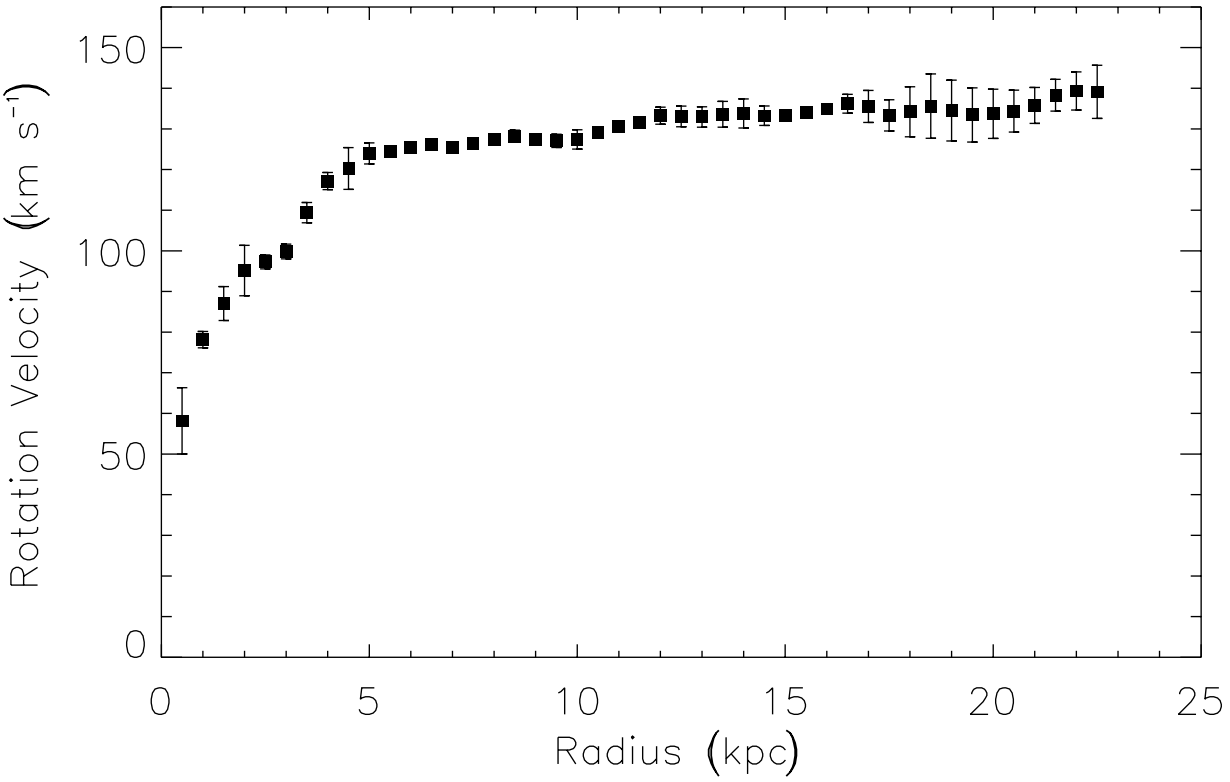

Figure 1.1: Rotation curve of the spiral galaxy NGC 2403. Figure adapted from Fraternali et al. (2002). The curve is mostly flat out to large radii, indicating that something other than the visible matter is contributing to the rotation velocity.

gas cloud orbits at its own velocity. A rotation curve is the relation between the velocity of the orbit and its distance from the center of the galaxy.

For bodies in rotation about a point source, such as the planets about the sun, the velocity decreases as $r^{-\frac{1}{2}}$. This is easily derived: the acceleration of the orbiting body due to the central mass is

$$a = \frac{GM}{r^2}, \tag{1.3}$$

directed inward, with M the mass of the central body. For a circular orbit, this must equal

the centripetal acceleration, $a = v^2/r$: thus,

$$v = \left(\frac{GM}{r}\right)^{\frac{1}{2}}. \tag{1.4}$$

While not point-sources, the distribution of stars and gas is centrally concentrated, and the visible matter alone should lead to a similarly decreasing rotation curve, though more shallow. What Rubin observed, however, was that the rotation curve in the disk of spiral galaxies was flat, and remained so out to great distances. This cannot be accounted for by the visible matter alone. These observations implied the existence of a halo of unobserved matter, many times more massive than the galaxy alone, with a distribution that is roughly isothermal, $\rho \propto r^{-2}$ (the profile which produces flat rotation curves), in shape.

Since then, there have been many other observations indicating the existence of dark matter. Dwarf spheroidal galaxies are small, dim galaxies with few stars. While the stars in such a galaxy are not in ordered rotation as they are in a spiral, the velocity dispersion, the width of the distribution of velocities, measures the mass of the galaxy in a similar manner to rotation curves. The measurements of the velocity dispersion in the galaxies present the same conclusion as spiral rotation curves: there is a great deal of unobserved matter in galaxies.

Observations of the dynamics of galaxies and clusters are not the only evidence for dark matter. The signature of dark matter is also present in the power spectrum of the cosmic microwave background (CMB).

The CMB is a relic of the early universe. In the first 370 kyr of the universe, the temperature was high enough that almost all hydrogen was ionized into protons and electrons. In this hot soup of plasma, a photon could not travel great distances before interacting with an electron and being scattered in a random direction. Eventually, however, the universe cooled to the point where the density of free electrons was low enough that the photons ceased to frequently scatter, and could travel freely. These photons now form the CMB. The time of last scattering, or the redshift of the CMB photons, is $z \approx 1100$.

The temperature of the CMB is extremely uniform. The variation about the average temperature of 2.736 K is on the order of only 1 part in 10^5. The power spectrum is the

measure of this small temperature variation as a function of scale on the sky. The positions of the peaks in the power spectrum, the scales where the variation reaches a maximum, indicate that the total density of matter is $\Omega_{m,0} = 0.27$, but that that of baryonic matter is only $\Omega_{b,0} = 0.05$—less than a fifth of the total. Thus, the majority of matter must be something other than baryonic, and it must be dark.

Primordial abundances of light elements are also evidence for dark matter. Formed during a brief period in the early universe, the abundance of these elements (primarily helium, with small amounts of deuterium and lithium) to hydrogen is sensitive to the density of baryonic matter. The measured abundances indicate a baryon density of $\Omega_{b,0} = 0.04 \pm 0.01$, in agreement with the CMB data.

Gravitational lensing observations provide yet more support for the existence of dark matter. Gravity bends the path of light as it does matter, so if an object, such as a galaxy, lies behind a large mass, such as a galaxy cluster, the image of the object will be distorted. From many of these distorted images, it is possible to reconstruct the mass distribution of the lensing object.

The classic example of a gravitational lensing observation in support of dark matter is the Bullet Cluster (see figure 1.2). This is actually a pair of colliding clusters, in which the galaxies of each cluster, being mostly empty space and widely separated, have passed through each other without effect. The hot gas which forms the intracluster medium of the clusters, however, has collided and stopped in between the two groups of galaxies. As the intracluster medium makes up the majority of visible matter in a cluster, the mass distribution should largely trace this gas. Gravitational lensing, however, reveals that the matter is concentrated in two lobes, centered on each group of galaxies. Thus, most of the mass of the cluster must be invisible and, since there was no collision that stopped it in the middle, must interact only through gravity—in other words, it must be dark matter.

1.2 Dark Matter Halos

1.2.1 Hierarchical Structure Formation

The picture of the universe, then, is one in which visible galaxies and clusters of galaxies reside within invisible dark matter halos. Simulations show these halos are denser knots

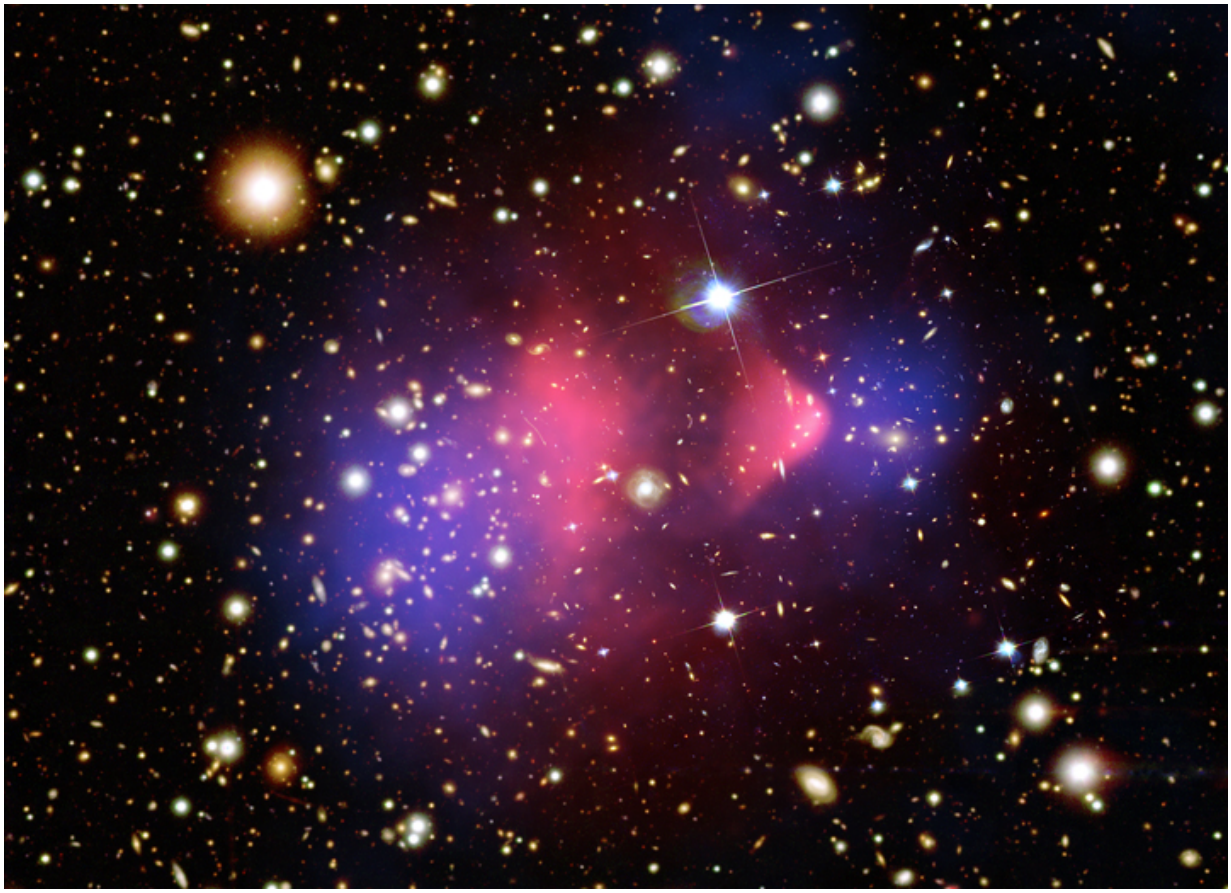

Figure 1.2: The Bullet Cluster. The pink clumps are the hot gas which makes up the bulk of the visible matter in the cluster. It is offset from primary concentrations of mass, shown in blue, inferred from gravitational lensing, indicating that most of the mass is in a form that is not visible: dark matter. Image credit: X-ray: NASA/CXC/CfA/M.Markevitch et al.; Optical: NASA/STScI; Magellan/U.Arizona/D.Clowe et al.; Lensing Map: NASA/STScI; ESO WFI; Magellan/U.Arizona/D.Clowe et al.

within walls and filaments of dark matter, which surround large, mostly empty voids. The question is, how did all this structure come to be?

In the early universe, matter was smoothly distributed; fluctuations about the average density were small, and Gaussian in form. As the universe aged, overdense regions, having slightly more mass than the average, attracted matter from less dense regions and grow in mass; and as they grew, they attracted yet more mass. Similarly, underdense regions lost matter to their higher density surroundings, less and less able to hold onto their matter as they become more underdense. The ultimate outcome of this process is the high density contrasts that are seen in the universe today, from the near-vacuum of the voids to the ultradense environment of neutron stars.

The presence of dark matter is critical to structure formation. Before recombination and the emission of the CMB, the constant scattering of photons off electrons meant baryonic matter was coupled to the photons. The effect of this coupling was to dampen out the fluctuations in the baryonic matter density. Only after the baryons decoupled from the photons were they free to collapse and form structure. Because of the dampening effect, however, there has not been enough time since the CMB for galaxies to have formed—if baryons were the only form of matter in the universe.

Dark matter, however, does not feel the influence of photons, and undergoes gravitational collapse from the start. By the time of the CMB, it has already begun to form structure, and baryonic matter, once free of the photons' interference, quickly falls into the potential wells of the gravitationally dominant dark matter. Dark matter thus provides a jump-start to the formation of baryonic structure.

The early growth of structure can be modeled analytically. The overdensity of a region of space is defined as

$$\delta = \frac{\rho - \rho_b}{\rho_b} \tag{1.5}$$

where ρ_b is the background density. The mathematics of Gaussian fluctuations are well understood, and as long as the fluctuations are small, $\delta \ll 1$, linear perturbation theory can be used to follow their growth. The fluctuations grow linearly with scale factor, independent of the magnitude of the fluctuation.

The density field can be decomposed into Fourier components $\delta_{\vec{k}}$ in comoving wavevector $\vec{k}$. Because of the linearity of the growth, each component grows independently of any other. The original power spectrum of the fluctuations (the magnitude of the variation of the components as a function of wavenumber $|k|$) in the very, very early universe is a power law with index ~ 1. In other words, the density variations are small on large scales, and large on small scales. Although the power spectrum undergoes evolution before significant structure formation takes place, the pattern of increasing density variation with decreasing scale still holds true. Structure is thus formed on the smallest scales first, with the scale of structures growing larger as the fluctuations on larger scales become large. This bottom-up process is called *hierarchical structure formation*.

The small perturbation approach works in the linear regime ($\delta \lesssim 0.1$), and can be extended with approximations to the quasi-linear regime ($0.1 \lesssim \delta < 1$). On small scales, however, structure is highly non-linear. Halos represent overdensities $\delta \gtrsim 200$. In order to model anything but the largest scales (which are still linear at the present day), it is necessary to turn to N-body simulations.

In N-body simulations, a realization of the random initial density fluctuations as discrete particles is generated. The gravitational forces between the particles are calculated and used to integrate the motion of the particles forward (see chapter 2 for further discussion). In this way, the evolution of the fluctuations in the non-linear regime can be followed.

1.2.2 The Nature and Formation of Halos

While halos are highly non-linear objects, there are approximations which can be used to model their formation and make statements about their properties. The spherical collapse model of Gunn & Gott (1972) considers the evolution of an isolated spherical overdensity in a flat, matter-only universe (sometimes called and Einstein-de Sitter, or EdS universe). Note that while the universe does contain other components, EdS is a good approximation at early times, when matter dominates and Λ is small.

Initially, the overdensity expands with the rest of the universe. The gravity of the sphere, however, slows this expansion until, at the turnaround time t_{ta}, it stops and the sphere begins to recollapse. Formally, it will recollapse into a singularity of infinite density at the center at $t_{col} = 2t_{ta}$. This time corresponds to a critical linear overdensity (the

overdensity of the region, had it continued to grow according the linear approximation) of $\delta_c \sim 1.69$.

However, real overdensities are neither perfectly spherically symmetric nor isolated. The matter will acquire angular momentum and deviate from this ideal behaviour. Instead, the overdensity will only partly collapse and will virialize, i.e. reach a quasi-equilibrium state. This virialized structure is a halo. The radius of this halo, the *virial radius* r_{vir}, will be roughly half that of the radius at turnaround. Although the time for this virialization to occur is not well-defined, it is usually taken to occur at the time the region would have collapsed into a singularity. At this point, the region will have an (real) overdensity relative to the background of $\Delta_c = 18\pi^2 \sim 178$.

This spherical collapse model allows for an estimation of the abundance of collapsed halos, first derived by Press & Schechter (1974). For a given smoothing length R, the amount of matter in collapsed halos, equivalent to the fraction of matter in regions of that size with linear overdensity $\delta \geq \delta_c$, can be calculated from the statistics of the initial fluctuations and the linear growth rate. The difference between the collapsed fraction on a scale $R\,(M)$ and $R\,(M + dM)$ can be taken to collapse into halos of mass M to $M + dM$. The Sheth-Tormen halo mass function(Sheth et al., 2001), a refinement of Press-Schechter, for a $50\,h^{-1}$Mpc side box in a $\Omega_\Lambda = 0.7$, $\Omega_m = 0.3$, $h_0 = 0.7$ cosmology is shown in figure 1.3.

While both Press-Schechter and the Spherical collapse models are only approximations, they do provide a useful analytic starting point for understanding halo properties.

From simulations, it is found that all halos, regardless of size, are well fit by a single profile. This profile is known as the NFW profile (after the authors, Navarro, Frenk, and White), and has the form

$$\rho\,(r) = \frac{\rho_s {r_s}^3}{r\,(r_s + r)^2} \tag{1.6}$$

(Navarro et al., 1997). r_s is the scale radius of the halo, where the logarithmic slope of the profile is the same as that of the isothermal profile, -2. Interior to this radius, the slope becomes shallower, $\rho \propto r^{-1}$, while exterior to it it is steeper, $\rho \propto r^{-3}$. That the middle region of the profile is roughly isothermal agrees well with the observation of flat galaxy rotation curves (see section 1.1.3). There is evidence that real halos do not follow the NFW profile in the innermost regions, being less shallow, possibly due to the influence of the baryonic component which resides there (i.e. a galaxy)(Taylor & Navarro, 2001; van

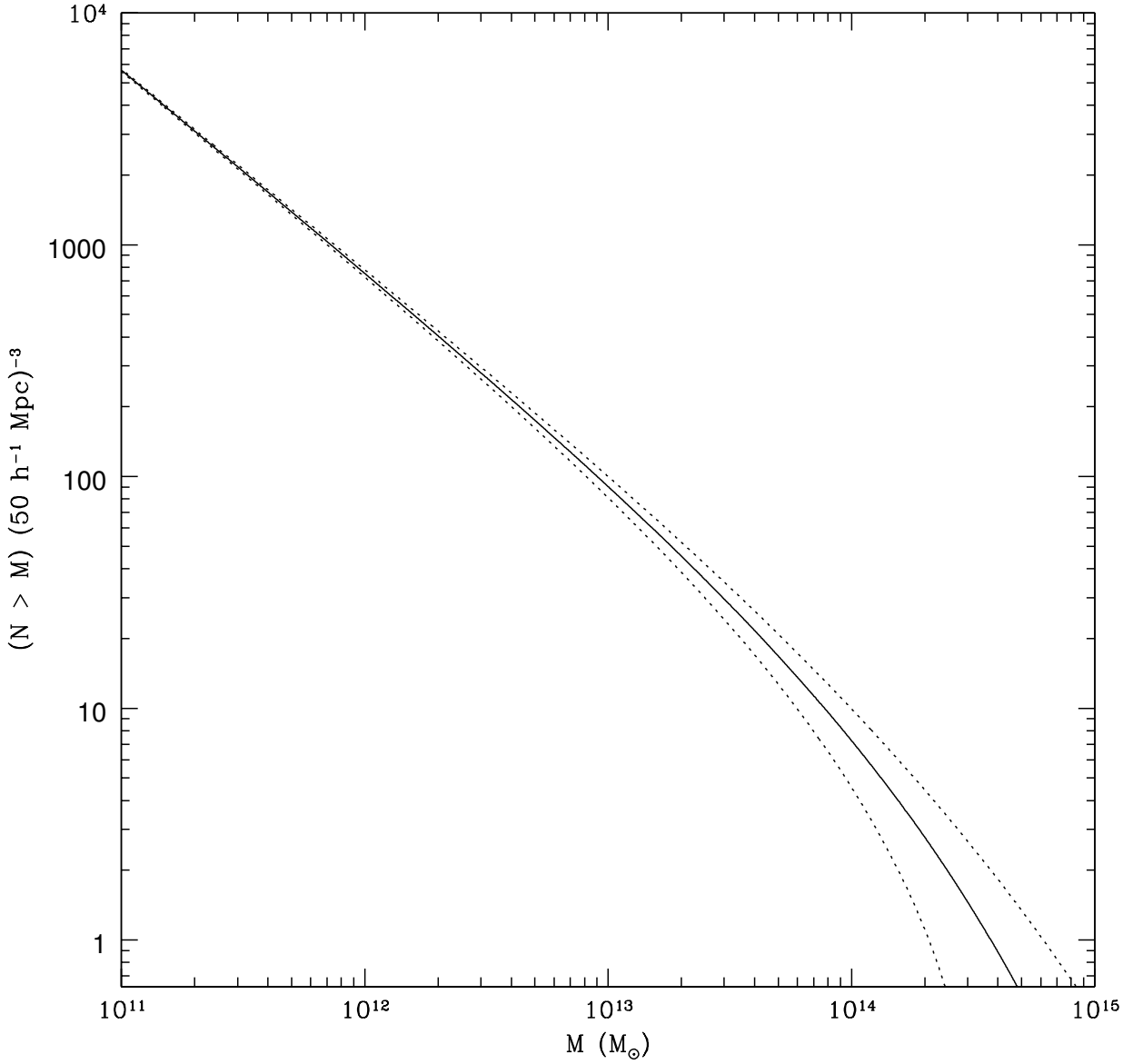

Figure 1.3: The Sheth-Tormen halo mass function for a $50\,h^{-1}$Mpc side box. Solid line is the average relation over all such boxes; the dotted lines are the 1σ box-to-box variation.

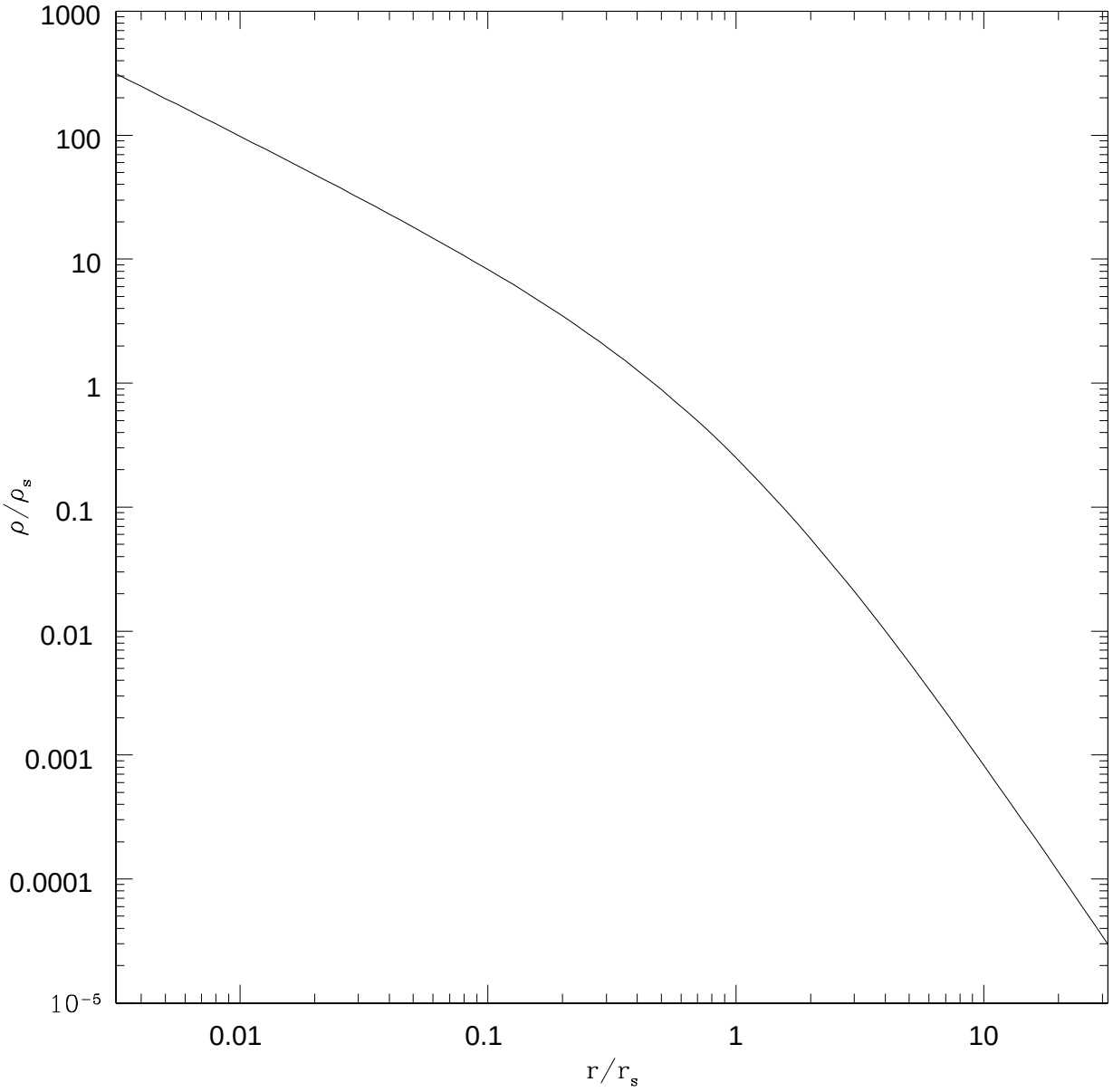

Figure 1.4: The shape of the NFW profile.

den Bosch & Swaters, 2001).

For a given NFW profile, the concentration parameter can be defined as

$$c = \frac{r_{vir}}{r_s}. \tag{1.7}$$

The higher the concentration, the more compact and dense the central region of the halo. The concentration is also connected to the age of the halo and its recent merger history.

1.2.3 Halo Mergers and Substructure

Halos are not static structures. They are constantly growing through the accretion of matter from the surrounding regions. The mass of a halo through time is referred to as its *mass accretion history*. The mass accretion history of a typical cluster-scale halo is shown in figure 1.5. The growth of a halo consists of two phases, an early period of rapid growth followed by slower accretion.

The mass accretion history allows us to define the age of a halo. Young halos have accreted much of their mass recently, while old halos have been mostly assembled for a long period of time. It is usual to define the age of a halo as the redshift at which a certain fraction of the mass is already assembled, e.g. z_{50} for 50%.

There is a connection between concentration and age. Rapidly growing halos have shallow density profiles ($c \sim 4$). When a halo is growing slowly, however, matter is mostly added to the periphery, without affecting the shape of the profile, and the concentration increases. Thus, in general, the older the halo, the higher the concentration.

The mass added to the halo does not just consist of "free" matter accreting smoothly onto the halo: part of it is already in the form of other virialized halos. When two halos join together, it is referred to as a merger.

The primary characteristic of a halo merger is the merger ratio, the ratio of the masses of the two halos. Based on the merger ratio, mergers can be grouped into two categories: major mergers, in which the masses of the halos are comparable, and minor mergers, in which one halo is much larger than the other. Though the dividing line between the two is arbitrary, it is often taken as a merger ratio of $1:3$.

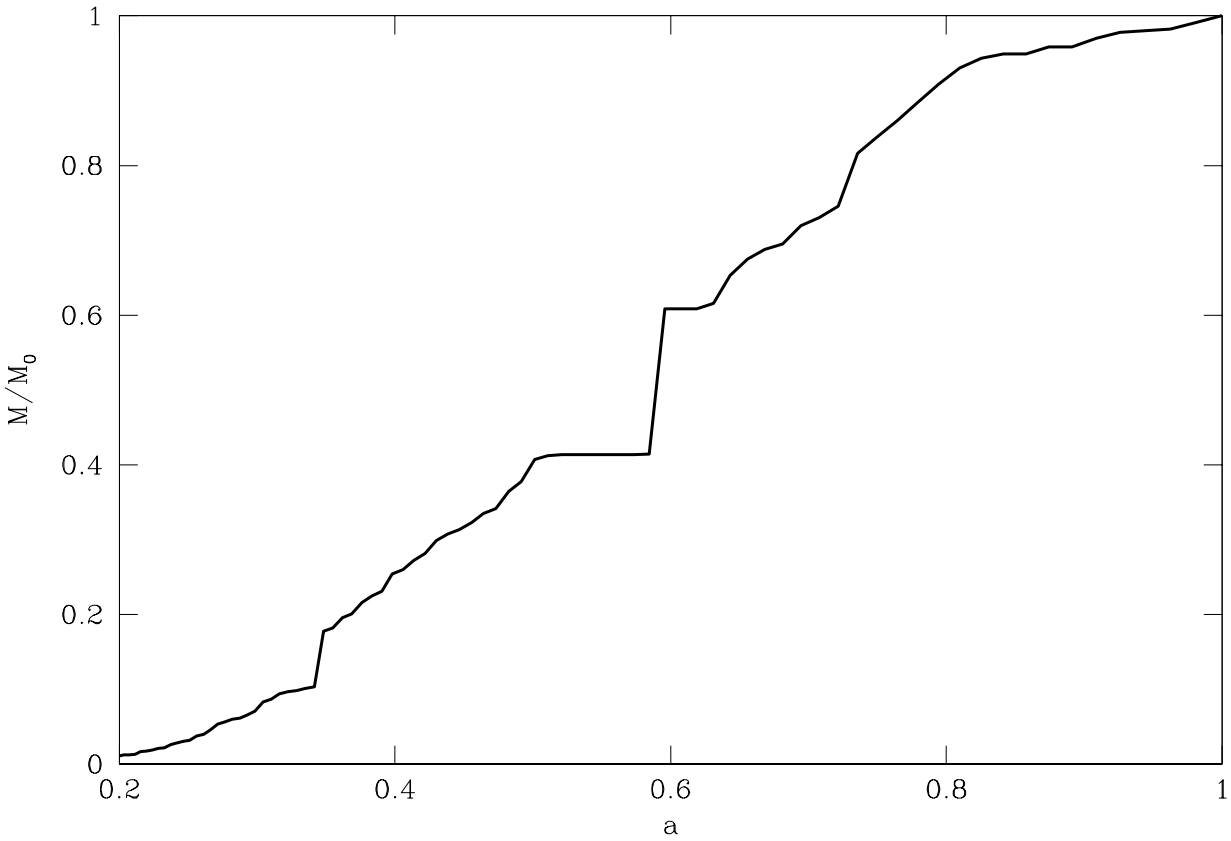

Figure 1.5: Example of the mass accretion history of a cluster-scale halo from one of our simulations, with $z_{50} \approx 0.67$. The change from fast to slow growth occurs at $a \approx 0.8$. Note the sudden jumps in mass that represent major mergers at $a \approx 0.35$ and $a \approx 0.6$.

When one halo merges into another, the outer regions of the smaller halo are stripped away and added to the larger. The dense core of the smaller halo is tightly bound, however, and can continue to exist as a distinct structure within the main halo: a subhalo. These subhalos may have subhalos of their own (sub-subhalos), and so forth. If there is a galaxy in the smaller halo before the merger, it will continue to reside within the subhalo. In a galaxy cluster, each of the satellite galaxies resides in its own subhalo.

1.3 The Stellar-Halo Mass Relation

Galaxy formation is a messy process, involving gas physics, star formation, the interaction of magnetic fields, feedback from active galactic nuclei, winds from supernovae, and other complicated elements which are difficult to model accurately, if at all. In contrast, the formation of dark matter halos is much simpler, dependent only on gravity, and so can be understood much more easily. It is helpful, then, to look for correlations between the properties of galaxies and the halos that host them.

One of the most basic properties of galaxies and halos that can be compared are the masses. It is reasonable to expect that halos with larger masses M_h should host galaxies with larger stellar masses $M_\star$, and this is indeed the case. The average relationship between the two, using the terminology of Leauthaud et al. (2012) (L12 hereafter), is the stellar-to-halo mass relation (SHMR hereafter).

The SHMR can be expressed as the relation between masses, but it can also be cast in terms of the ratio $M_h/M_\star$. How this quantity varies with stellar mass is perhaps more enlightening, as it represents the efficiency with which the galaxy can form and accrete stars and thus relates directly to galaxy formation.

Results from galaxies in the field (Blanton et al., 2008; Moster et al., 2010; Behroozi et al., 2010; More et al., 2011; Leauthaud et al., 2012) using a variety of techniques (weak lensing, abundance matching, satellite kinematics, the Tully-Fisher relation) reveal that the ratio between halo and stellar mass is not constant across halo or stellar mass (see figure 1.6). For galaxies around the mass of the Milky Way ($M_\star \sim 4.5 \times 10^{10}\,\mathrm{M}_\odot$), $M_h/M_\star$ reaches a minimum, and the efficiency of accumulating stellar mass is highest.

Above this mass, the efficiency rapidly decreases. While galaxies do not get much larger than the Milky Way, around an order of magnitude at most, the masses of the largest, cluster scale halos are three orders of magnitude greater in mass than that of the Milky Way.

The efficiency also decreases towards lower masses, though much more gradually than the high-mass end. Small galaxies can be extremely dark, with little mass in the form of stars.

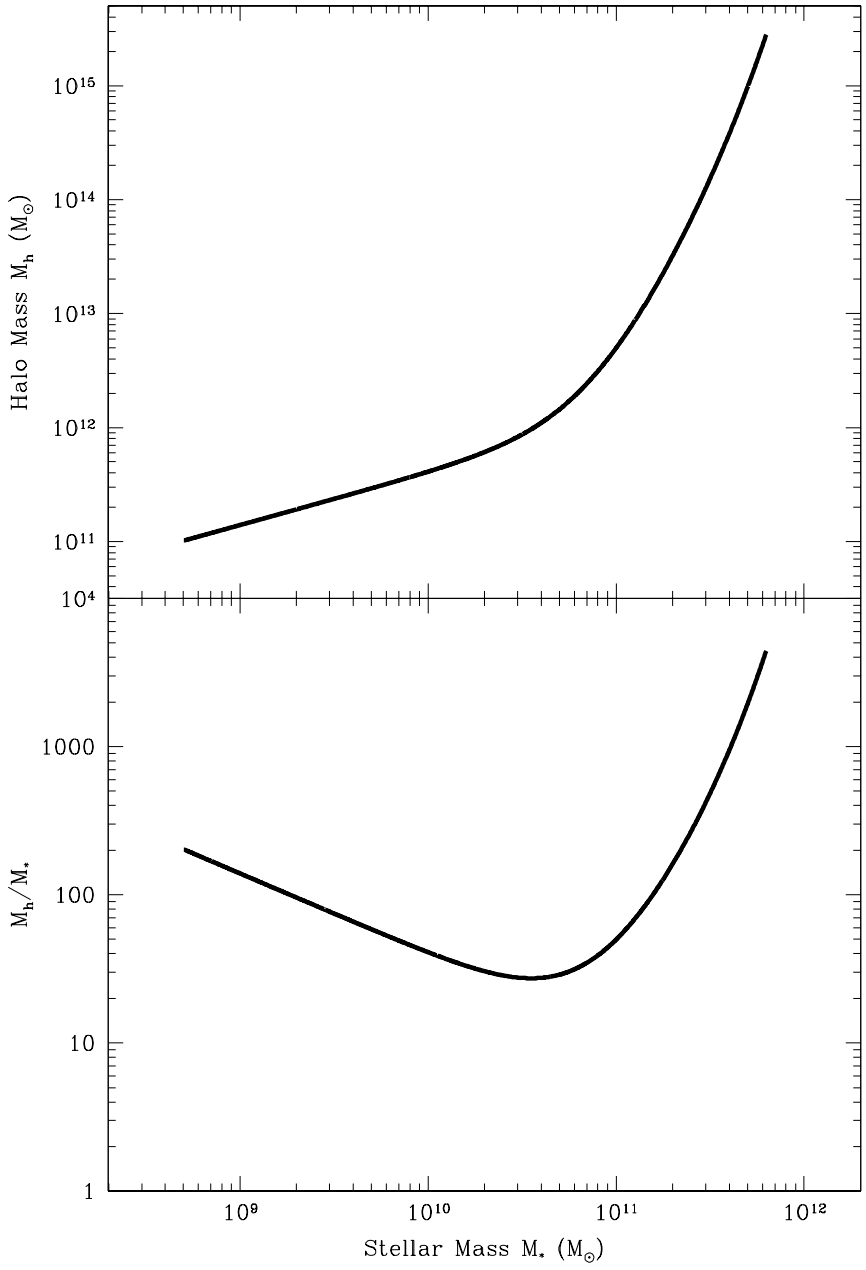

Figure 1.6: SHMR from Leauthaud et al. (2012) for the redshift bin centered at $z = 0.37$

It is also of interest to know how the SHMR evolves with redshift. L12 find a decrease in the mass at which the efficiency peaks from $z = 0.88$ to $z = 0.37$. Performing this analysis at high redshift, however, is difficult. Stellar masses bring with them large uncertainties, and measuring the halo masses directly, through lensing or kinematics, is often not feasible (Leauthaud et al., 2012). This is especially true at low mass and high redshift, where we would like to extend the relation. It is thus necessary to turn to other techniques.

1.3.1 Abundance Matching

Abundance matching is an alternative method of determining the SHMR, which does not require finding $M_\star$ and M_h for individual galaxies. Instead, it makes use of the galaxy stellar mass function (the abundance of galaxies by stellar mass) and the halo mass function (the abundance of halos by mass). The former can be found from observations, the latter from simulations. With these relations in hand, it then matches the galaxies and halos in a one-to-one manner, assuming the largest galaxy resides in the largest halo, the second largest galaxy in the second largest halo, and so on.

Abundance matching has already been used to determine the global SHMR of halos in the field (Behroozi et al., 2010; Moster et al., 2010) at low redshift. To investigate the SHMR at higher redshift, we can use the same technique, but applied to the subhalos and satellite galaxies of a low-z cluster. Such objects are the descendants of independent systems at higher redshift. Star formation eventually ceases after they merge into the larger system (Hansen et al., 2009; Peng et al., 2010), although there are complications such as how abruptly it ceases and if there is a burst of star formation triggered by the merger. Nevertheless, the satellite galaxies can serve as a window into the nature of galaxies of an earlier stage in the universe, and down to much lower masses than can be directly observed at high redshift. To do this, we also need simulations of sufficient resolution to resolve the corresponding substructure.

1.3.2 This Work

The Virgo cluster is the nearest galaxy cluster, at a distance of (16.5 ± 1.2) Mpc (Mei et al., 2007). It is comprised of two main subclusters, with the more massive one centered on the elliptical galaxy M87, and the smaller ($\sim 25\,\%$ the mass of the larger) centered on M49.

The more massive subcluster has a mass of $M_{200,c} = 1.4\text{–}4.2 \times 10^{14}\,\mathrm{M}_\odot$ (Urban et al., 2011; McLaughlin, 1999). This system provides the best opportunity to study the evolution of galaxies in a cluster environment down to low mass.

This work makes use of the Next Generation Virgo Survey (NGVS) and high-resolution simulations of Virgo Cluster-like halos to perform abundance matching on subhalos. We can do a simple one-to-one matching using all subhalos and satellites, which explores how the galaxy-subhalo mass relation differs from its field halo counterpart.

The benefit of this approach is that it allows us to probe the SHMR at higher redshift, to much lower masses than could otherwise be achieved. The low mass regime is an area of particular interest. Since Moore et al. (1999) and Klypin et al. (1999), it has been recognized that for galaxy scale halos, simulations predict a much greater amount of substructure than is in fact observed in the Local Group in the form of satellite galaxies of the Milky Way and M31. This deficit is referred to as the missing satellite problem. To resolve this, one must postulate either that the ΛCDM model is deficient and the substructure present in simulations is spurious, or that the substructure exists, but most of the time does not form galaxies through which it can be traced. A good determination of the relationship between halo and stellar mass at low masses is necessary to resolve this issue.

In order to relate the subhalo SHMR to the global SHMR at higher redshift in more than general terms, we must be able to relate some observable property of the subhalos and galaxies to the redshift at which they merged with the main system. We take a first step in this direction by investigating the relations of velocity and radius to age.

In principal, both velocity and radius should exhibit an age gradient, with faster/outer subhalos having merged more recently than slower/inner ones. Mergers complicate this, as they can disturb these gradients. Thus, we attempt to characterize the degree to which material is mixed during mergers, and how this depends on the merger ratio.

This thesis is organized as follows. In chapter 2, we discuss the codes used in running and processing out simulations. Chapter 3 provides an overview of the simulations, and chapter 4 presents the results of the abundance matching using them and NGVS. Chapter 5 deals with the relation between mergers and mixing. Finally, we summarize our conclusions in chapter 6.

Chapter 2

Codes and Simulation

To run and process cosmological simulations requires the use of many different computer codes, some written ourselves and some of them kindly provided by others. Here we describe these codes.

2.1 N-body Simulation

To simulate the formation of dark matter structure, one begins with a realization of the density fluctuations within some comoving volume at high redshift, discretized into equal mass particles with appropriate positions and velocities (see section 2.2). The number of particles used, or, equivalently, the mass of each individual particle, determines the resolution limit, the mass of the smallest structures that can be reliably discerned in the simulation.

The motions of the particles are then integrated forward to whatever redshift is desired, typically $z = 0$, with the accelerations at each timestep coming from the gravitational interactions of the particles. In cosmological simulations, the expansion of the universe is also simulated.

Although only a limited volume is simulated, there is obviously much matter outside the box which would contribute to the force experienced by the particles, particularly at the edges. This difficulty is solved through the use of periodic boundary conditions. The edges of the box wrap around, so that particles leaving the box on one side reappear in

the same position on the other. As the universe is homogeneous on the scale of typically simulated volumes, this is a valid approximation.

As the particles in the simulation do not represent actual particles, but extended mass distributions, it is necessary to modify the equation of gravity by softening the force at small distances. This prevents close two-body interactions which would occur if they were treated as point particles, resulting in unphysical relaxation. This softening is characterized by a softening length ϵ, which is related to the distance between particles beyond which the force of gravity is Newtonian. For example, one simple form of softening used is Plummer softening, which modifies the gravitational potential of a particle to be

$$\phi = -\frac{GM}{\sqrt{r^2 + \epsilon^2}}.$$

At large separations $r \gg \epsilon$, the potential and force is approximately Newtonian, but at close separations the force between two particles is reduced. More commonly used than the simple Plummer softening are spline softenings, which reproduce the Newtonian potential exactly beyond some multiple of the softening length. A spline softening is used in the N-body code we employ (see below).

The integration of motion cannot be performed with infinite precision in time. Instead, it must be performed in discreet time steps. This time resolution introduces small errors in the integration. Smaller time steps result in smaller errors, but also longer run times. One technique to improve the situation is the use of adaptive time steps. Each particle uses its own, individual time step, which varies according to how fast its phase-space position is changing. Thus, particles undergoing low accelerations, with slowly changing velocities, can use long timesteps, and short timesteps can be used for only those particles for which it is required.

In principle, one could calculate the force of every particle on every other particle to determine the accelerations. This "direct summation" method, however, is impractical for large numbers of particles, as the number of calculations required goes as the square of the number of particles. To overcome this difficulty, a number of techniques can be used to approximate the force using algorithms which scale better. Two of these are tree methods and particle mesh methods.

In tree methods, the particles are organized into a tree based on position. Each node in the tree holds the first few (or one) terms of the multipole expansion of the collection of

particles it corresponds to, allowing them to be treated together in a single step. To calculate the force on each particle, one then walks the tree, and for each node determines if it is far enough away, relative to the volume represented by the node, for the node "particle" to be a sufficiently good approximation. If not, the child nodes are considered in the same way, and so on and so forth until the individual particles are reached, if necessary. In this way, particles close by are treated individually, while those far away are treated as single large, aggregate groups.

Particle mesh methods use Fourier techniques on the distribution of particles to calculate the force at positions on a mesh placed over the box. This has the benefit of being very fast; however, for small distances on the scale of a mesh cell, it has poor force resolution.

The code used for our simulations is Gadget2, a popular N-body code, written by Volker Springel (Springel, 2005). Although capable of running simulations including gas physics to simulate the formation of galaxies, we make use only of the dark matter gravitational capabilities. Gadget2 is a massively parallel code, allowing the work load to be spread over a large number of processors, using adaptive time stepping and a hybrid approach to calculating the particle interactions, with a tree method to used for the short-range forces and a mesh method for the long-range forces. The softening used is a spline softening, with the gravitational potential exactly Newtonian beyond 2.8ϵ, and the potential at zero separation Gm/ϵ as for Plummer softening. The softening length is defined in comoving units, and so increases in physical units as the simulation progresses.

Gadget2 also provides the ability to efficiently perform zoomed-in simulations (see section 2.3), and can output the state of the simulation (a "snapshot") at arbitrarily specified redshifts.

2.2 Initial Conditions

To run a simulation, one must start with initial conditions. These initial conditions represent a random realization of the density field in a volume at some early redshift, discretized into particles. These particles are given positions and velocities to mimic the underlying continuous distribution.

The redshift at which the simulation begins cannot be arbitrarily selected. One naturally wishes to start the simulation at as late a time as possible, so as to minimize the amount of computationally expensive simulation which must be performed. However, the density fluctuations must be evolved analytically up to the starting redshift, so it must be early enough for the analytic expressions to remain valid on the relevant mass scales.

The initial conditions for our simulations are generated using the Grafic2 and `LINGERS` codes, both written by Ed Bertschinger.

Given an input cosmology, `LINGERS` generates the corresponding power spectrum and evolves it through time. This power spectrum and the cosmology are passed to Grafic2, which generates a corresponding random density field. An initial Cartesian grid of N^3 particles is then distorted to reproduce this random density field.

The initial redshift is selected such that the rms fluctuations on scales corresponding to the mass of the particles is $\sigma(M_p) \lesssim 0.10$. This ensures that the lowest resolvable scales are still linear at the start of the simulation.

Grafic2 also provides the capability to generate multiscale initial conditions, with a subvolume being sampled by a larger number of less massive particles. This capability allows it to create initial conditions for resimulation (see section 2.3 below).

2.3 Resimulation

To correctly account for the effects of the environment on a halo requires simulating volumes substantially larger than that of the halo itself, but in order to resolve the detailed structure of the halo, one must use many low-mass particles. Simply running large, high-resolution simulations if often not practical, if even possible, and is in a sense wasteful. If one is only interested in a single halo, then all the extra time spend simulating regions far away from it at high resolution is unneeded.

The technique of resimulation, or zooming, is a solution to this dilemma. In resimulation, only the regions of interest are simulated at high resolution. Regions far away

are simulated at much lower resolution, only high enough to capture their effect on the structure of interest.

To resimulate a halo (or other region of interest), one first runs a simulation at low resolution. A halo from the final output this simulation is then selected for more detailed investigation. Those particles which are "part of" the halo are then traced back to the initial conditions, defining a resimulation volume.

It is not enough to simply take those only particles which are actually in the halo, however. A single low-resolution particle may have the same mass as potentially hundreds of the high-resolution particles used to resimulate the halo. If one of these massive particles winds up in the halo, it will have an unphysically disruptive effect. To prevent this, more than just the halo itself must be resimulated. It is necessary to take a larger volume around the halo, and use all the particles within it to define the resimulation volume. In this way, the disruptive high-mass particles are kept away from the region of interest (i.e. the halo).

The particles within this volume, however selected, are removed from the initial conditions and replaced with a larger number of higher resolution particles. The power on the scales probed by the low-resolution particles is maintained within the volume, and power is added on smaller scales in keeping with original power spectrum.

The simulation is then rerun with these new initial conditions, now with particles of two different masses. The result of this second run is a halo of high resolution embedded within a low resolution simulation, and which takes much less time and memory to run than rerunning the whole simulation at higher resolution.

2.4 Halo Finding

The output of a N-body simulation is only the particles representing the underlying continuous matter distribution. To investigate the halos within the simulation, it is necessary to find and define which particles compose them in some manner. There are two basic approaches to halo finding: friends-of-friends (FOF) and spherical overdensity (SO). We use both methods in this work.

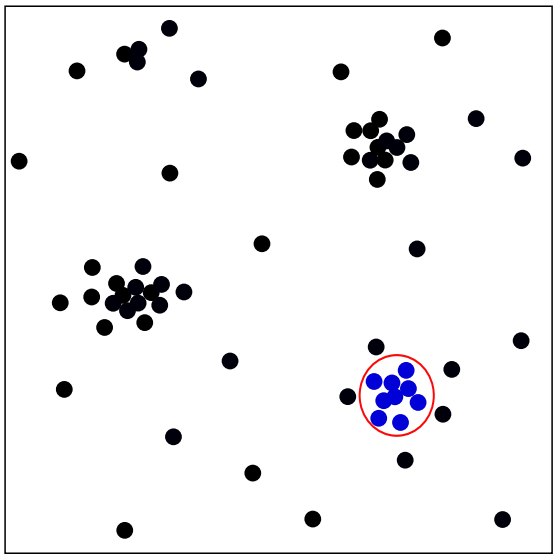

(a) A halo is selected from the final snapshot of a normal, low-resolution simulation.

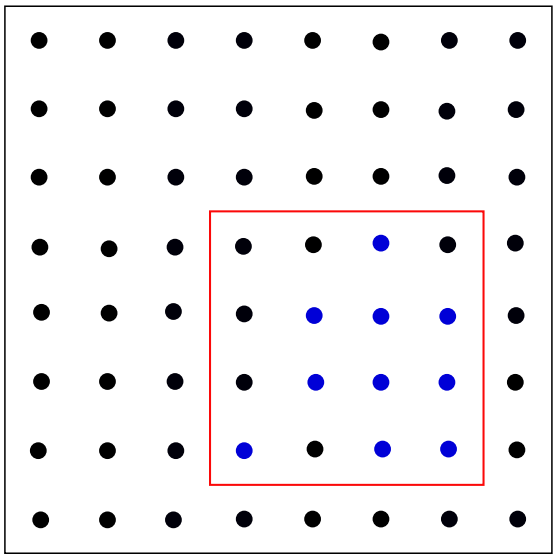

(b) The particles of the halo are found in the initial conditions, and the volume containing them determined.

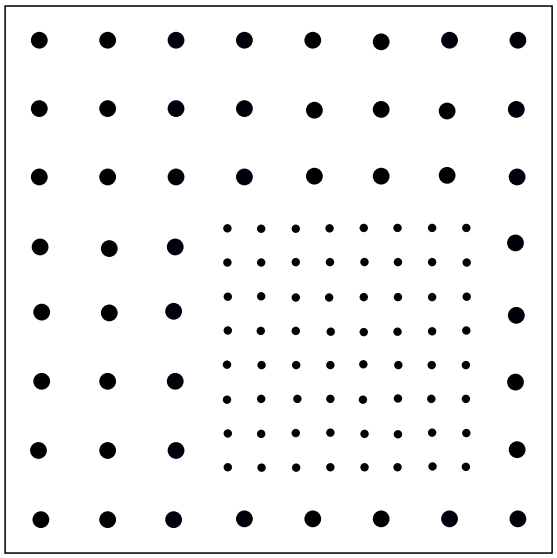

(c) The massive, low-resolution particles within the resimulation volume are replaced by a larger number of lighter, higher resolution particles.

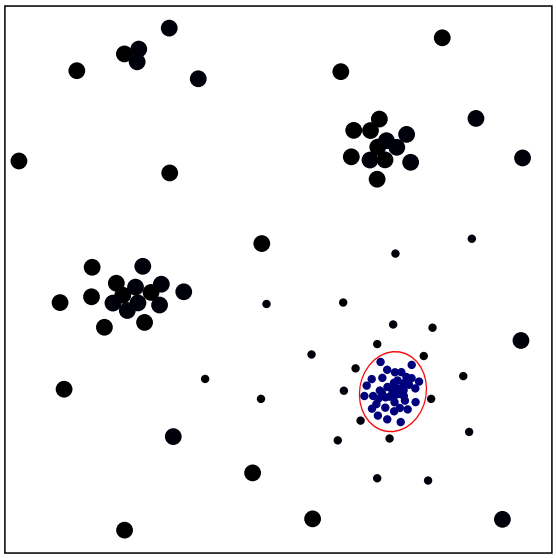

(d) The simulation is rerun with these new initial conditions, resulting in a much higher resolution halo.

Figure 2.1: A schematic view of resimulation.

2.4.1 Friends-of-Friends

The FOF method is a geometric method, based on the proximity of particles to each other. It is characterized by a *linking length*, usually expressed as a fraction of the mean inter-particle separation. Particles closer than this distance are considered linked. A halo consists of all particles that are linked together, directly or through links to other particles. By choosing an appropriate linking length, a structure corresponding to a virialized halo is recovered.

Because of the simplicity of the algorithm, FOF is a fast halo finding method. It also has the ability to find halos of arbitrary shapes. However, the method is also prone to joining halos via so-called linking bridges, where, due to chance alignment, a chain of particles exists in which they are close enough to each other to form a link between two otherwise separate halos.

We use a basic FOF code originally written by University of Washington HPCC group (http://www-hpcc.astro.washington.edu), modified to work with resimulated Gadget2 snapshots. We select a linking length of 0.2 times the mean inter-particle separation, which is the typical value used for FOF.

2.4.2 Spherical Overdensity: Amiga Halo Finder

In the SO approach to halo finding, density peaks in the simulation are first identified. A sphere is taken around each of the peaks, and the radius is increased until the mean overdensity reaches some threshold.

The SO approach has the benefit of recovering halos representing a well-defined and selectable overdensity, and unlike the basic FOF algorithm, can in principle recover substructure as well. However, any halos that are found are spherical by definition, while real halos are usually significantly triaxial.

The SO-like code we use is the Amiga Halo Finder (AHF), written by Knollmann & Knebe (2009). In essence, it is an SO code which also removes unbound particles from the halos. It naturally recovers substructure and sub-substructure, and calculates a number of

useful halo properties. It is, however, very memory intensive and slow to run.

We use AHF's built-in virial overdensity capability, which automatically calculates and uses the actual virial overdensity for the appropriate cosmology for its threshold density.

2.5 Merger Trees

In order to investigate the history of halos, it is necessary not only to find the halos in the simulation snapshots, but also to connect the halos between snapshots. A description of how a halo has evolved through the simulation, what halos it corresponds to in earlier snapshots and how these merged together to form the final halo, is called a merger tree.

We wrote a code to construct these merger trees. For each halo in each snapshot, it determines a progenitor and a descendant. These are defined as the halo in the preceding or following snapshot, respectively, which shares the most particles with the halo in question.

By following the chain of a halo's progenitors (i.e. its progenitor, its progenitor's progenitor, etc.), the evolution of a halo, e.g. its mass accretion history, can be traced. Where two different halos have the same descendant, a merger occurs.

Determining the ancestry of subhalos was done in a slightly different matter. For each subhalo, its primary ancestor, the halo with which it shares the most particles (the greatest *overlap*), was determined in each snapshot. The nature of the relation between the subhalo and its ancestor was also characterized as independent, non-independent, or merged, which are defined as follows.

An independent ancestor of a subhalo is one which corresponds to the subhalo when it was an independent halo in the field (*progenitor* hereafter), and which is not contaminated by the false merger with another halo via linking bridge or other confounding effects. To be considered independent, no other subhalo may have a particle overlap with the ancestor halo of greater than 1/3 the subhalo of interest's overlap with it (i.e. it is not substantially interfered with).

A merged ancestor is one which is assumed to represent an earlier host halo of the subhalo, i.e. the case where the subhalo was at that time merely a subhalo of the ancestor. This is considered to be the case when another subhalo has an overlap with the ancestor greater than 3 times the overlap of the subhalo in question.

Ancestors which are neither independent nor merged are non-independent. Such an ancestor represents an instance where the subhalo progenitor has not properly merged into another halo, but cannot be considered isolated either. This can occur, for instance, if a linking bridge exists between two similar mass halos which are otherwise independent. An FOF halo of this sort cannot be reliably used for estimates of the subhalo at earlier times.

With a list of primary ancestors for a subhalo thus obtained, we can define several properties characterizing the independent progenitor of the subhalo. The maximum mass, M_{max}, is the largest mass the subhalo ever had when it was an independent halo, defined as the largest mass among its ancestors. The infall mass, M_{inf}, is the mass the halo's progenitor had immediately before infall, taken as the mass of the last independent ancestor.

When determining these two masses, we further remove the influence of false mergers in the following way. Moving forward from the earliest independent ancestor, whenever the mass of the progenitor increases by more than 1/3 between snapshots, the current state is saved. Whenever the mass decreases by more than 1/4, which almost certainly represents the end of a false merger, we revert to the last saved state and exclude all ancestors between then and the timestep under considerations. In this way, a temporary (and artificial) jump in mass from a false merger does not incorrectly set the maximum mass.

We can also determine the merger redshift, when the subhalo last existed as an independent halo. This is defined as the redshift of the last ancestor which is not a merged ancestor.

It is not always possible to find M_{inf} and M_{max}, especially for the smallest halos. It can be that a subhalo's progenitor is never independent by the criteria outlined above. This is not a significant problem, however, affecting less than 1 % of subhalos overall, and almost none above ~ 200 particles.

Chapter 3

Simulations of Virgo-like Clusters

To perform abundance matching using the Virgo Cluster and NGVS, we require simulations of cluster-scale halos of similar mass. Given the low masses to which NGVS can probe, we need these simulations to be able to resolve substructure down to similarly low masses. In order to reach these low resolutions, we use the technique of resimulation. This chapter presents an overview of these simulations.

3.1 The Simulations

The simulations are of a cubical volume $140\,h^{-1}$Mpc side box. We used a cosmology based on WMAP-7 (Komatsu et al., 2011), with $\Omega_b = 0.045$, $\Omega_c = 0.226$, $\Omega_\Lambda = 0.729$, $H_0 = 70.3\,\mathrm{km\,s^{-1}\,Mpc}$, $n = 0.966$, $\sigma_8 = 0.809$.

For both the initial simulation and the resimulations, we output 120 snapshots spaced evenly in $\log a$ between $z = 9$ and $z = 0$.

3.1.1 Initial Simulation

The initial, top-level simulation was run with 256^3 particles. With the chosen volume and cosmology, this yields a per-particle mass of $1.230\,197 \times 10^{10}\,h^{-1}\mathrm{M}_\odot$. The softening length

used was 0.02 times the mean inter-particle separation, $\epsilon = 10.9375\,h^{-1}$kpc in comoving units.

Once the simulation was complete, friends-of-friends was run on the final snapshot to find halos for resimulation.

3.1.2 Resimulated Halos

From the top-level simulation, candidate halos for resimulation were selected with a mass of $2 \times 10^{14}\,\mathrm{M}_\odot$ to $5 \times 10^{14}\,\mathrm{M}_\odot$, comparable to the mass of the Virgo cluster. In order to minimize interference from other large halos, any halo with a neighbouring halo within $3\,h^{-1}$Mpc of greater than 1/5 its mass was excluded from consideration. From the halos meeting these criteria, 10 were chosen for resimulation. These 10 halos represent a wide range of formation epochs and mass accretion histories (see figure 3.1).

Each of the halos was resimulated individually. For each halo, the rectangular volume containing the particles of the halo was determined. This box was then extended to twice the linear size, and all particles within this second volume chosen at the target of the resimulation. By choosing this volume, we ensured that all particles associated with the halo, out to roughly twice the virial radius, are captured by the resimulation, as well as providing a substantial buffer region to prevent the intrusion of the surrounding more massive particles into the halo proper.

The resimulations were performed with a factor of 1000 increase in mass resolution, the mass of the high-res particles being $1.230\,197 \times 10^7\,h^{-1}\mathrm{M}_\odot$. For the high-res particles, a softening length of 0.014 the mean high-res inter-particle separation was used, $\epsilon_{high} = 10.9375\,h^{-1}$kpc in comoving units. This softening length is consistent with the optimal softening length for the resolving of substructure as defined in Power et al. (2003), for halos of the selected mass range. The softening length used for the massive, low-res particles was the same as in the top-level simulation, $\epsilon_{low} = 10.9375\,h^{-1}$kpc.

A summary of the resimulated halos is presented in table 3.1. They contain from 8.8 to 24.4 million particles, equivalent to a mass of $1.54 \times 10^{14}\,\mathrm{M}_\odot$ to $4.28 \times 10^{14}\,\mathrm{M}_\odot$, and have from 2000 to almost 6000 resolved sub- and sub-sub-halos. A picture of each halo is shown

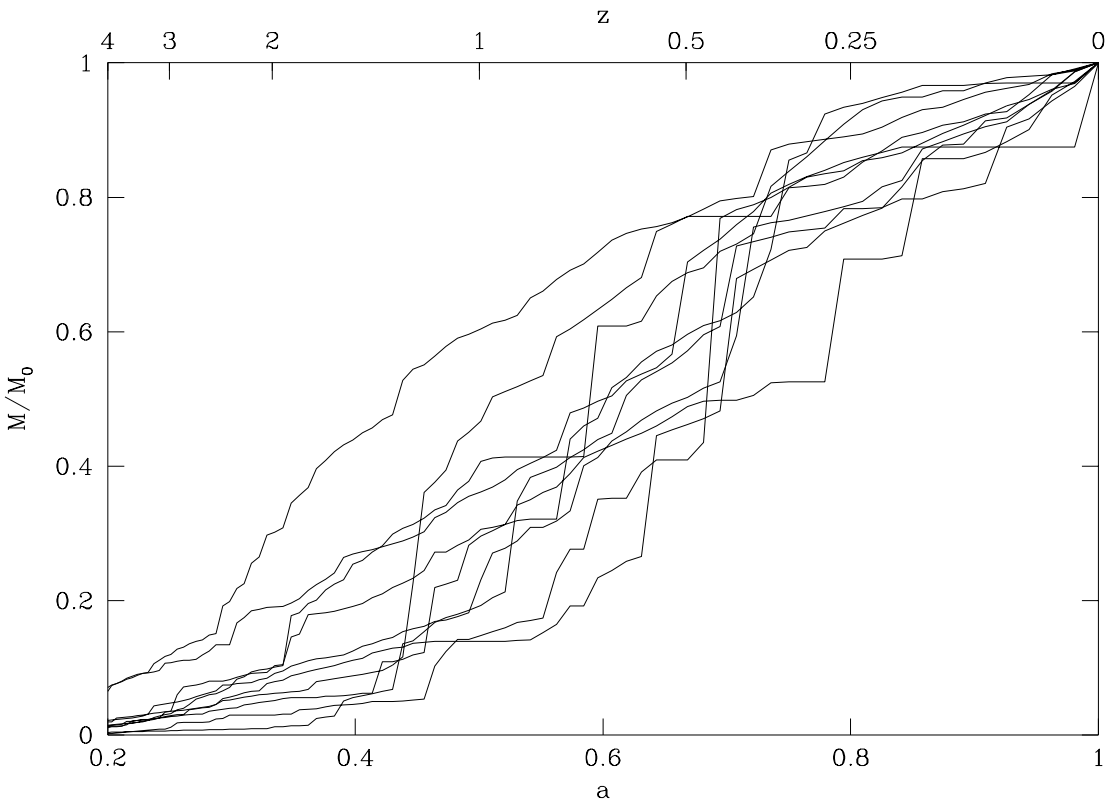

Figure 3.1: The mass accretion histories of the 10 resimulated halos. Masses are normalized to the mass at $z = 0$.

halo	$M_h\,(10^{14}\ \mathrm{M}_\odot)$	$N_{part}\,(10^6)$	N_{sub}	$r_{vir}\,(\mathrm{kpc})$	$v_c\,(\mathrm{km\ s^{-1}})$	c	z_{50}
3	3.67	20.9	5328	1868	954	4.1	0.42
6	3.66	20.9	4983	1867	986	5.4	0.69
7	2.04	11.7	2366	1536	907	9.8	1.30
15	2.03	11.6	2546	1534	827	6.1	0.99
20	2.39	13.7	3437	1619	843	4.9	0.67
24	2.69	15.4	3656	1685	883	5.1	0.52
27	1.54	8.8	2154	1400	841	10.6	0.39
29	4.28	24.4	5786	1967	1071	6.5	0.45
35	1.86	10.6	2009	1489	819	6.9	0.66
40	2.54	14.5	3756	1653	862	4.9	0.64

Table 3.1: Properties of the resimulated halos

in figure 3.2, showing the wide variety of structure present across the simulations.

3.1.3 Processing

To extract the resimulated halo and its substructure, AHF was run on the final snapshot. For the rest of the snapshots, we used the FOF finder to extract the halos.

The merger tree codes were then run on the main halo, finding the primary progenitors of its subhalos to find M_{max}, M_{inf}, and z_m for each subhalo.

As we wish to compare the halos of the simulations, which have different masses, to a single cluster (Virgo), it is necessary to scale all halos to a single mass. We therefore deal primarily in relative quantities, e.g. $M_{subhalo}/M_{host}$.

The NGVS survey, which we use to perform abundance matching in chapter 4, currently only covers the central $\sim 1.9 \times 1.9\,\mathrm{deg}^2$. To facilitate the comparison, we place the same constraint on the data we use from our simulations. Each resimulated halo is first projected along each of the x-, y-, and z-axes. In each projection, only those halos within the central $0.252r_{vir} \times 0.252r_{vir}$ square are included. This area corresponds to the completed region of NGVS, assuming (following NGVS) a distance to Virgo of 16.5 Mpc, $r_{200,c} = 1.55\,\mathrm{Mpc} = 5.38°$, and a concentration (using $r_{200,c}$) of 2.51. The group of 30 sets of subhalos thus defined comprises our data set for all of the following analysis in this and the next chapter, unless otherwise stated.

3.2 The Subhalo Population and Resolution Issues

Because the halos are being scaled to a common mass, the issue of resolution, which depends on particle count, is made more complicated. There is a factor of ~ 3 between the number of particles in the largest and smaller halos; so while the smallest halos (the subhalos of which drop below a given number of particles at the highest fractional mass) are suffering incompleteness from the effects of limited resolution, the largest halos are still comfortably above the resolution limit and complete.

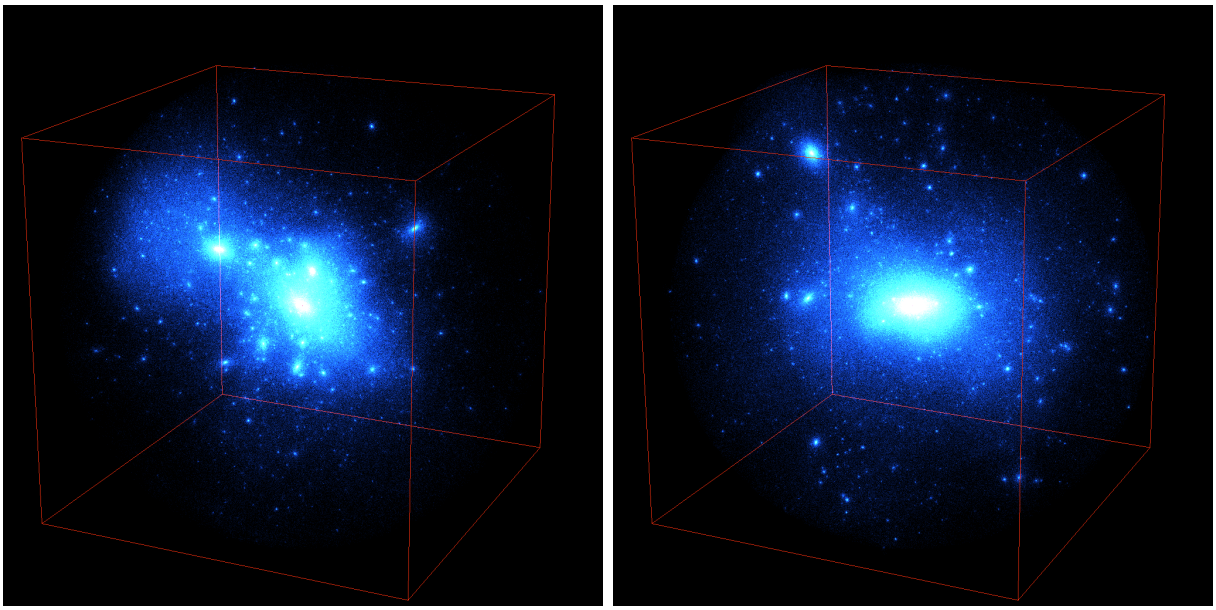

(a) halo 3

(b) halo 6

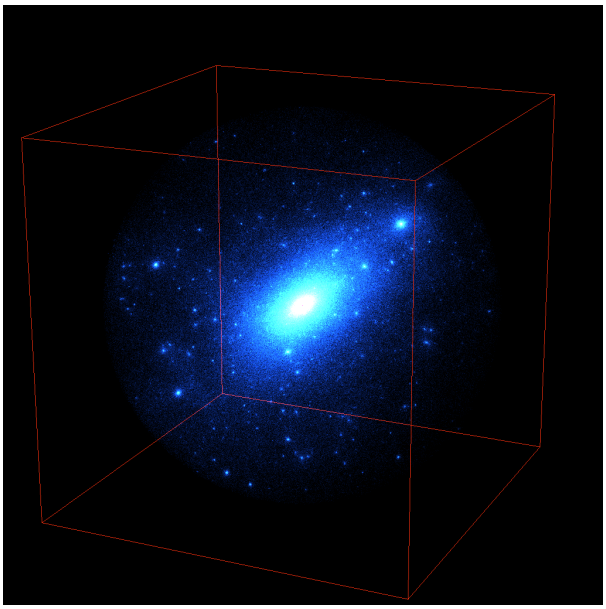

(c) halo 7

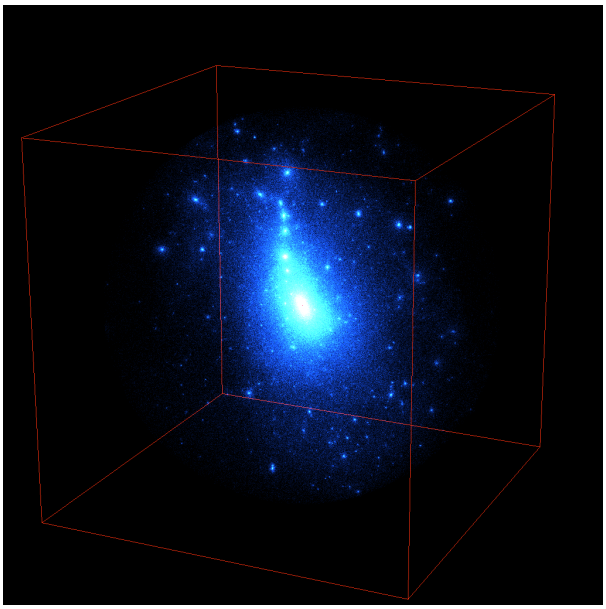

(d) halo 15

Figure 3.2: Halo images. The containing box is 3 Mpc on a side.

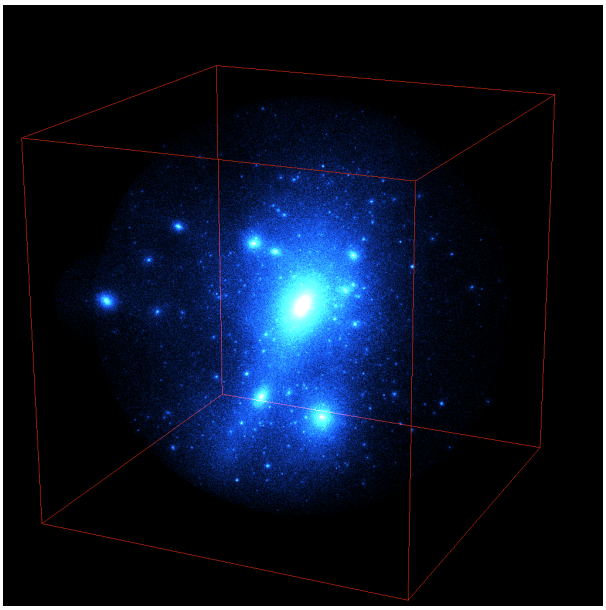

(e) halo 20

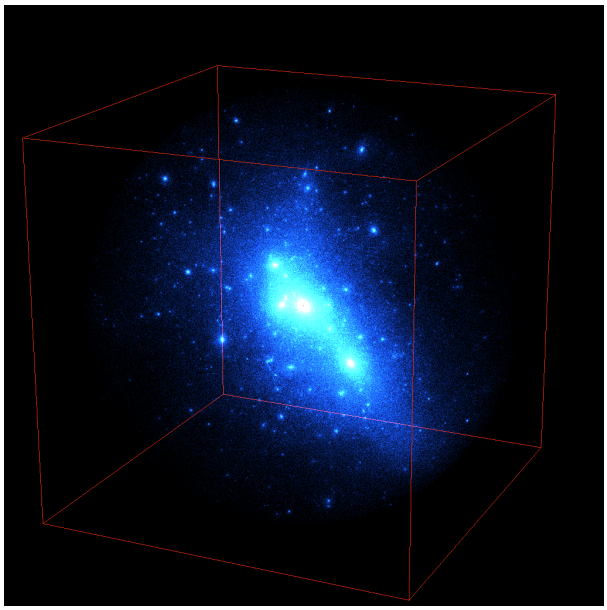

(f) halo 24

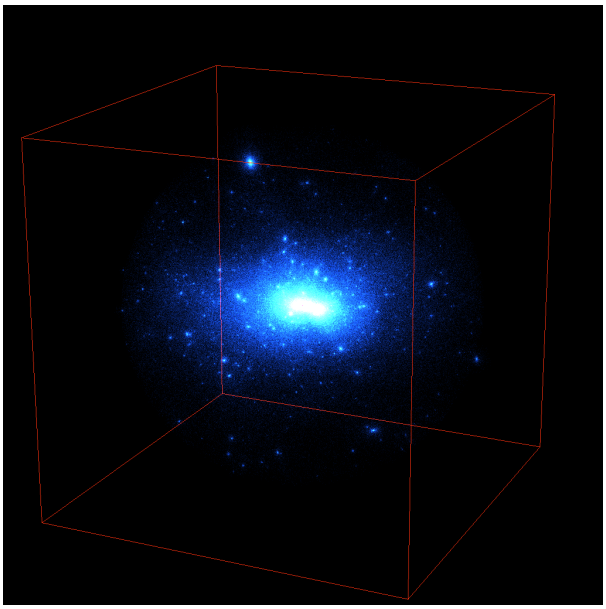

(g) halo 27

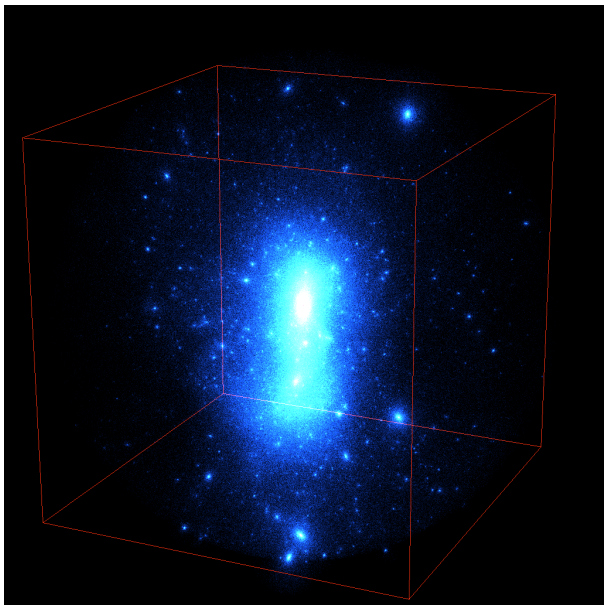

(h) halo 29

Figure 3.2: Halo images, continued

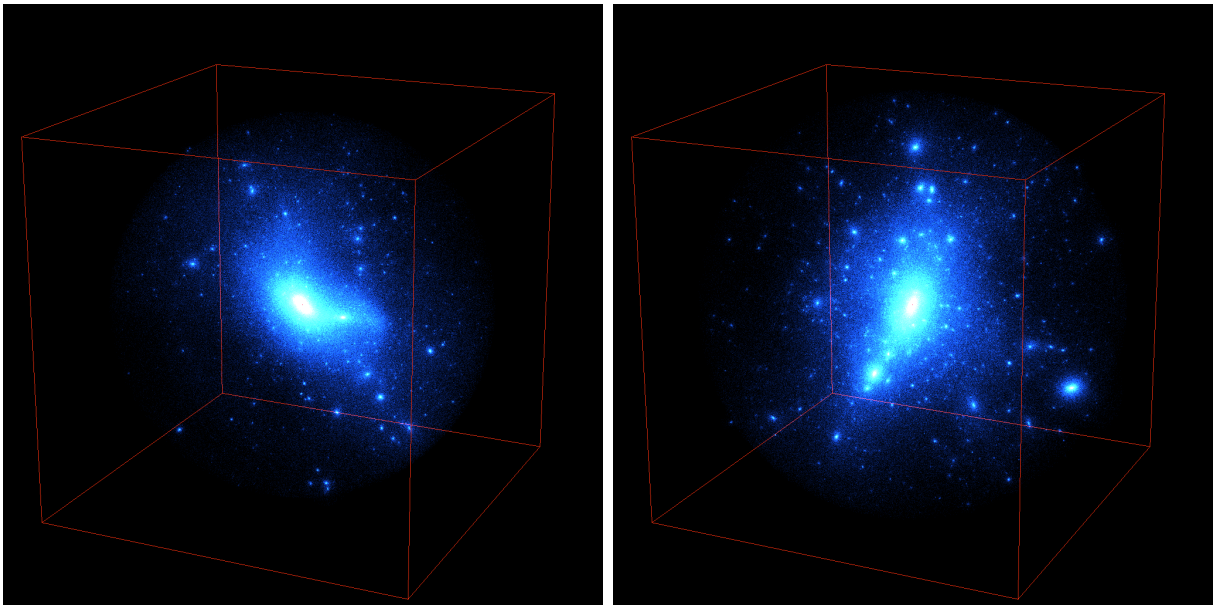

(i) halo 35 (j) halo 40

Figure 3.2: Halo images, continued

We can test the effect of resolution by examining the subhalo mass function (SHMF) of the halos. The SHMF is a cumulative count of halos above a given mass. Below a small fraction of the main halo's mass, this relation is a power law with an index slightly smaller than unity. Deviation from this power law indicates the incompleteness of subhalos below this mass.

All three SHMF have a similar form, roughly power law in shape, though with slightly different slopes and normalizations. The SHMF for M_{max} and M_{inf} are very similar, the latter being slightly shallower as, by definition, $M_{inf} \leq M_{max}$. The difference in normalization between these two and $M_{z=0}$ comes from both the striping of mass from the subhalos post-merger and the different definitions of mass (from the FOF codei, used in earlier timesteps, and AHF, used for the final one).

The $M_{z=0}$ SHMF begins to deviate from the power law behaviour at around $M_s = 7 \times 10^{-6} M_{host}$, corresponding to ~ 70 particle subhalos in the smallest main halos. For the lowest masses, some of this will come from limitations in AHF's ability to detect such small subhalos; but most of it will come from artificial relaxation of the subhalos. In fact,

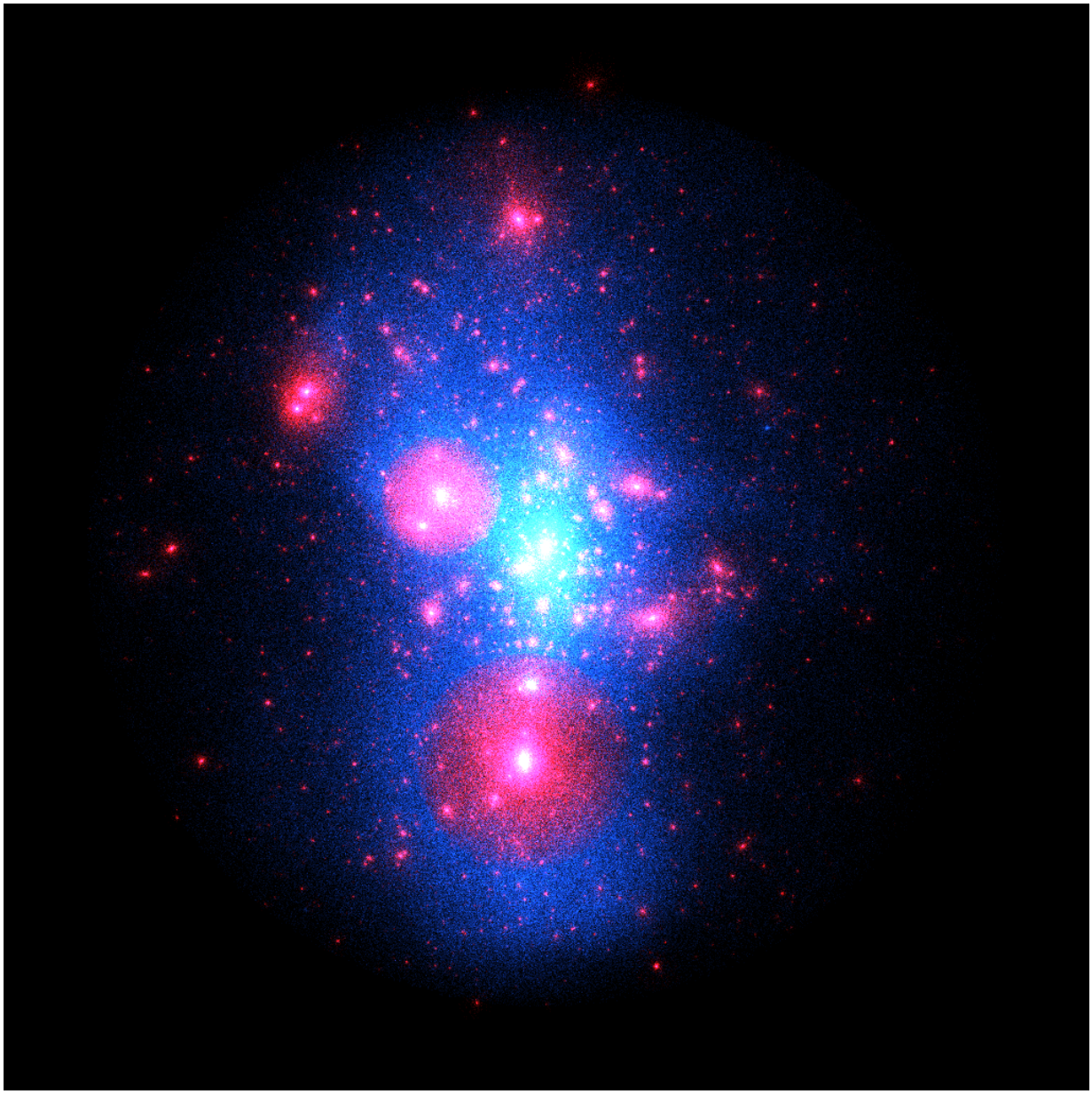

Figure 3.3: A more detailed view of halo 3, with the subhalos highlighted. Note that the high density in the central region make visually distinguishing subhalos there difficult with this coloration scheme.

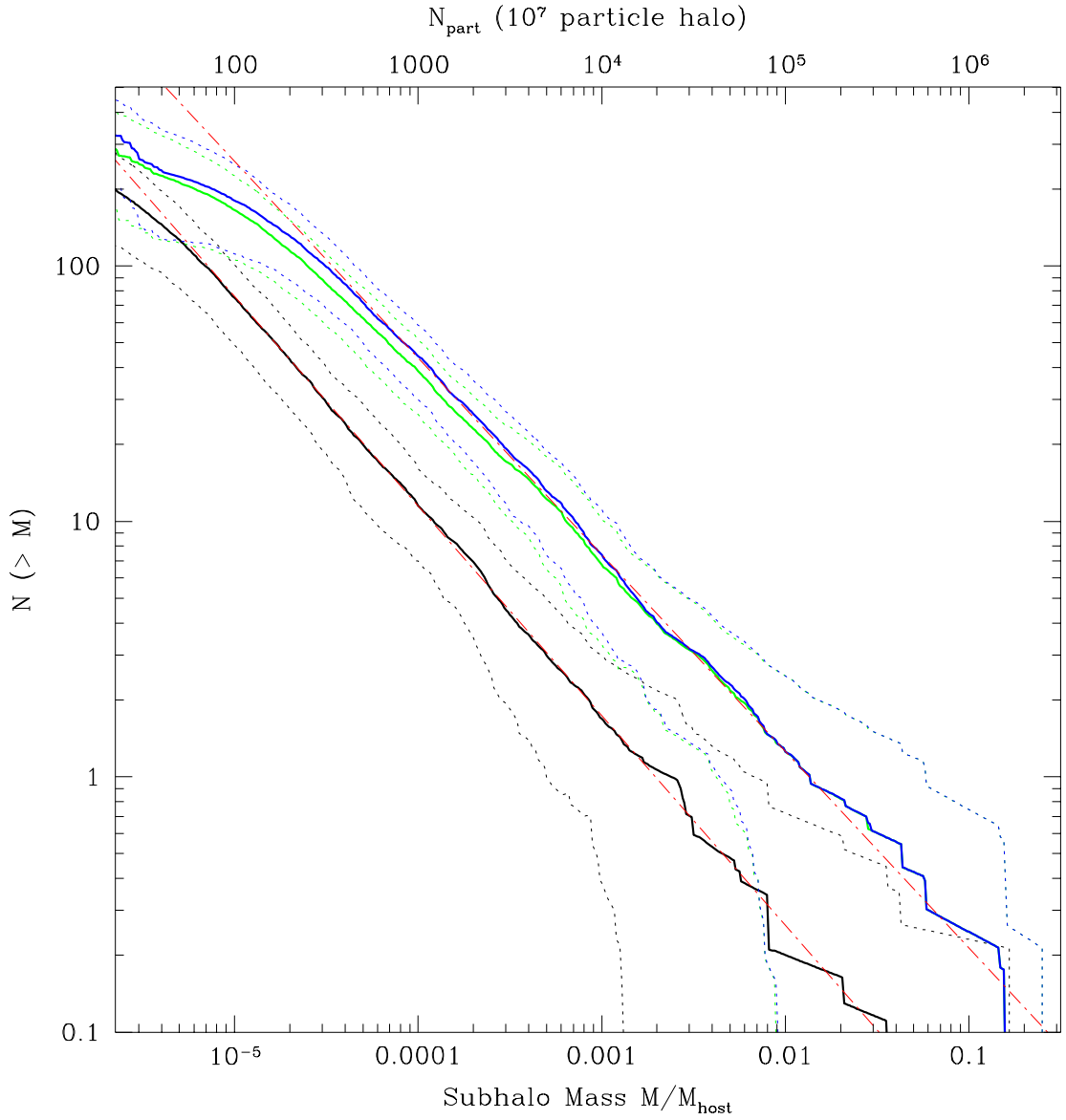

Figure 3.4: The subhalo mass function for the three mass definitions. Black, green, and blue solid lines are the mean SHMF for $M_{z=0}$, M_{inf}, and M_{max}, respectively. The dotted lines represent the 1σ variation about these means. The top axis shows the mass in terms of particles for comparison, for a 1×10^7 particle main halo. The red dot-dashed lines are power laws with slopes -0.82 (lower) and -0.78 (upper), corresponding to the slopes of the $M_{z=0}$ and M_{max} SHMF. For clarity, no power law fit is shown for M_{inf}, but the behaviour is very similar to M_{max}.

subhalos are likely to suffer artificial relaxation at particle counts higher than this limit; however, due to the scaling of the halos to a common mass, the effect of this will not appear above a (relative) mass for which the largest simulations are near to or at the actual particle limit as well.

The deviation from a power law for the M_{inf} and M_{max} SHMF occurs at around $M_s = 4 \times 10^{-5} M_{host}$, or ~ 400 particles in the smallest main halos. This is not directly a resolution issue, except at the very lowest masses where the FOF code runs into difficulties reliably detecting halos. Rather, it follows from the resolution limitation for the original subhalos. The much higher mass at which incompleteness sets in compared to $M_{z=0}$ is only partly due to the difference in normalizations. The amount of stripping a subhalo of a given mass has undergone since merging varies significantly from subhalo to subhalo, so the completeness of subhalos at a given mass will have an effect on the completeness of the progenitors at masses above that corresponding to the mean amount of stripping.

We therefore consider our results to be not limited by resolution above $M_s = 7 \times 10^{-6} M_{host}$ when derived from $M_{z=0}$, and $M_s = 4 \times 10^{-5} M_{host}$ for those derived from M_{inf} or M_{max}.

3.3 Velocity Age Gradient

We cannot observe the age of a subhalo directly. One thing we can measure, however, is its velocity relative to the center of the cluster, through the Doppler shift of the galaxy it contains. It is natural, then, to ask if there is any useful information to be gained from knowing the velocities of the subhalos. In principal, older subhalos, which are on lower energy orbits, ought to have lower velocities in general than younger subhalos which have just merged with the halo. We would like to know if such a relation can be recovered.

To do this, we divide the subhalos into three bins, based on their line-of-sight velocity relative to that of the main halo. The "low" velocity bin consists of those subhalos with $|v| \leq 0.5 v_c$, the "middle" bin for those with $0.5 v_c < |v| \leq 1.0 v_c$, and the "high" bin for $1.0 v_c < |v|$.

Figure 3.5 shows the SHMF for the three velocity bins using the final mass $M_{z=0}$. All three are remarkably similar in both slope and normalization (though there is the

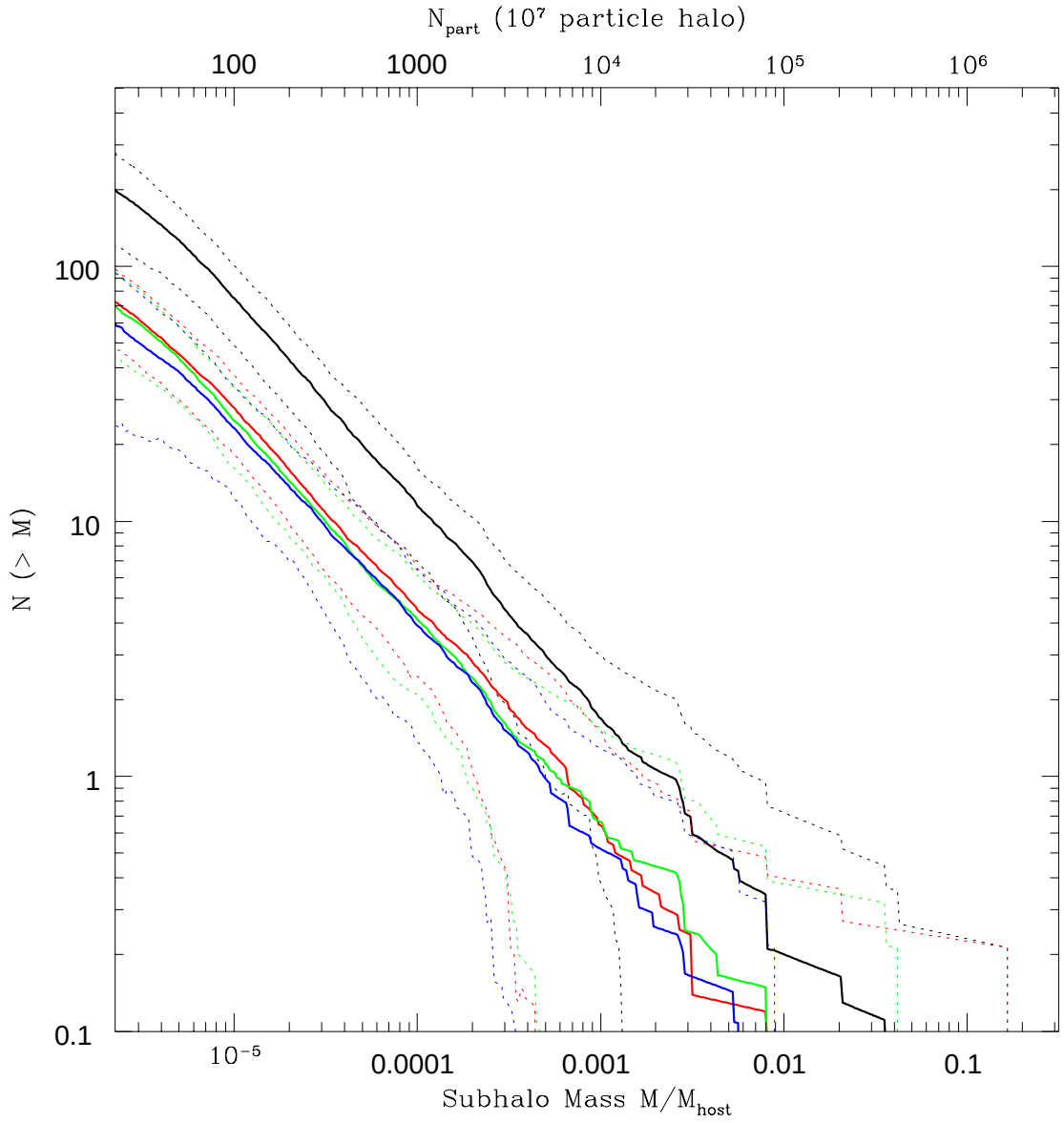

Figure 3.5: Subhalo mass function with velocity binning, using the final mass $M_{z=0}$. Red, green, and blue lines are the mean SHMF for the low, middle, and high velocity bins. Black is the total of the three bins. Dotted lines are the 1σ variation about these means.

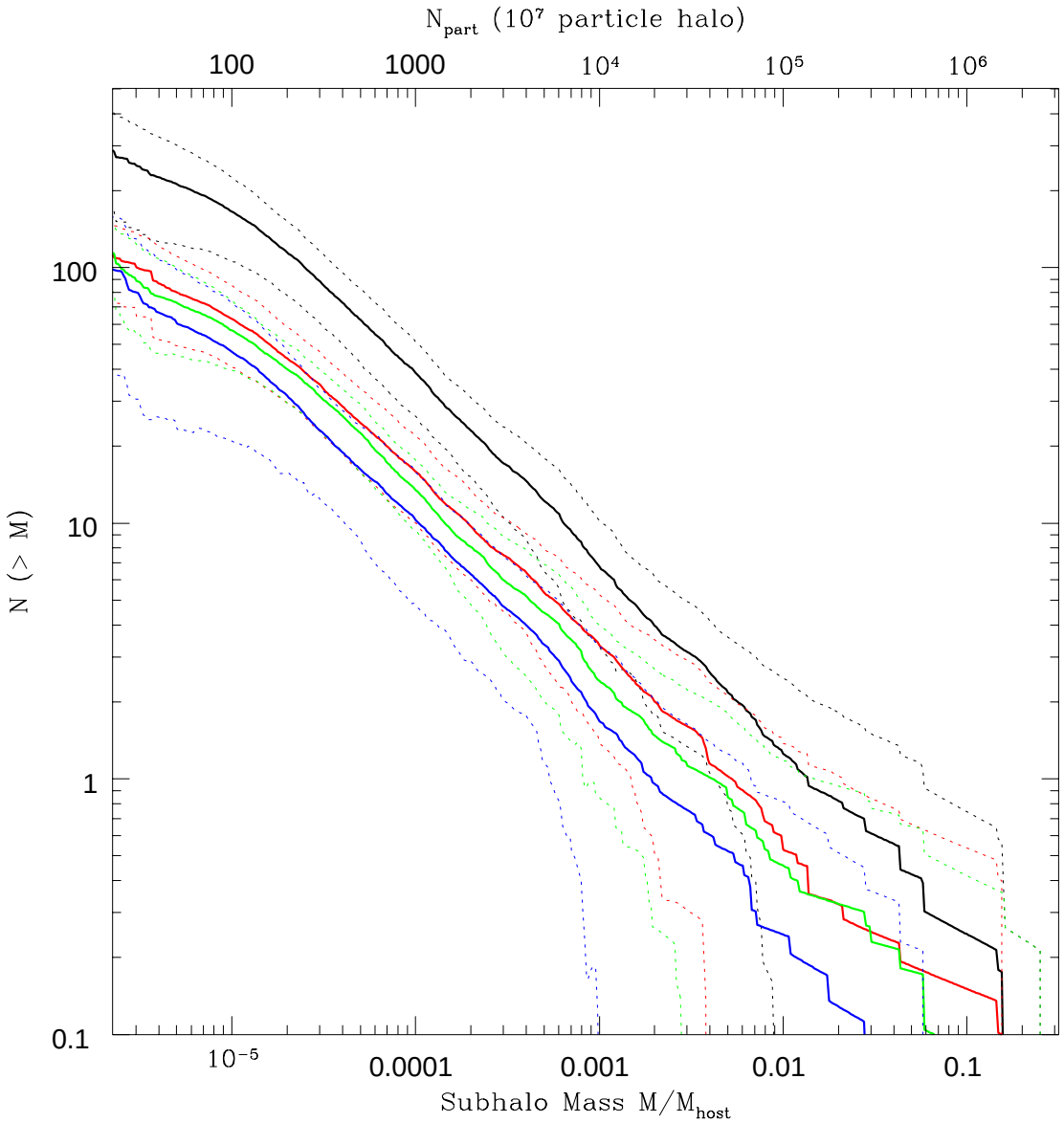

Figure 3.6: As figure 3.5, but using the infall mass M_{inf}.

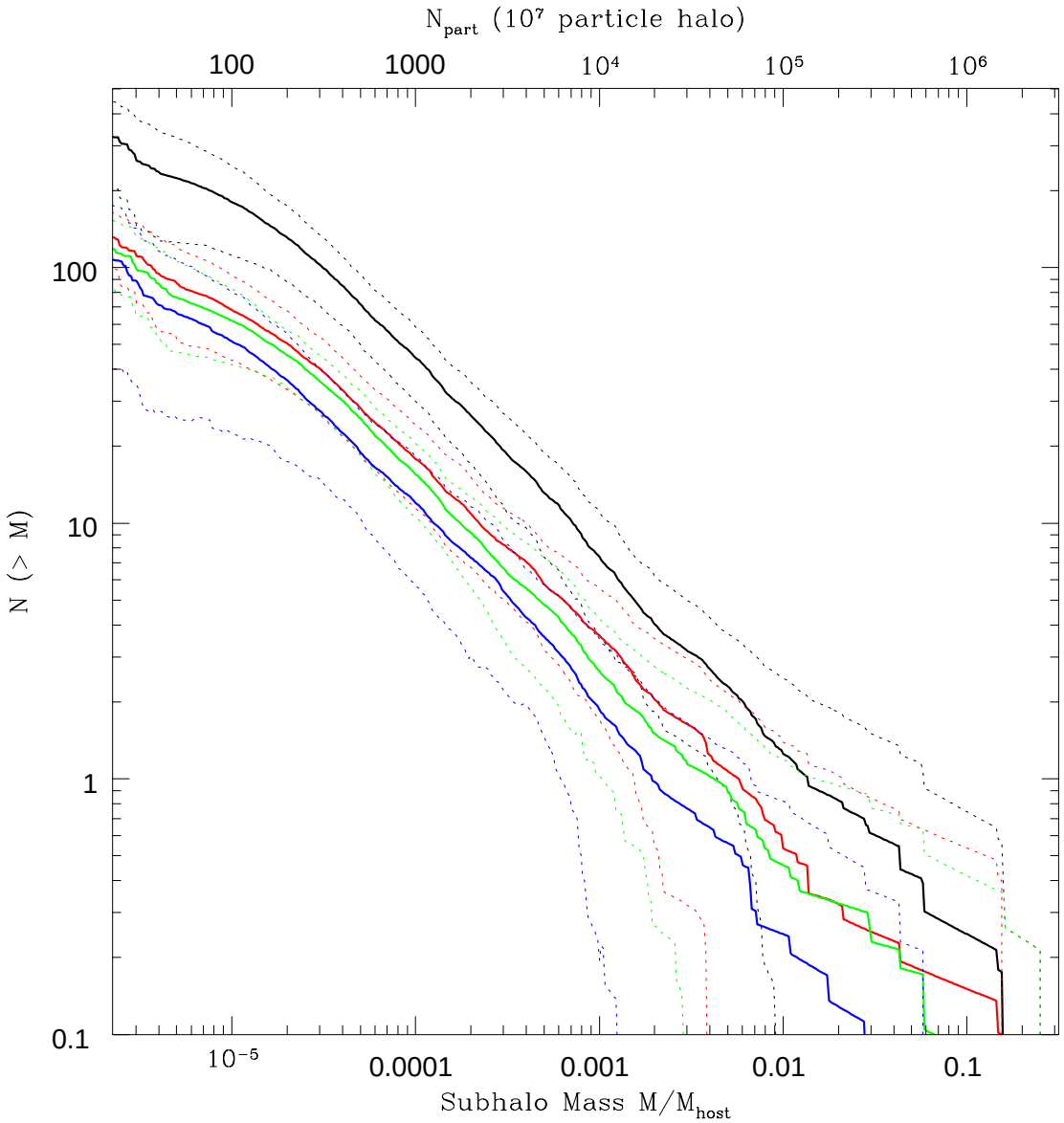

Figure 3.7: As figure 3.5, but using the maximum mass M_{max}.

suggestion of the middle velocity bin SHMF being slightly steeper). This is a useful property, as the presence of a difference in the stellar mass functions over the same three bins immediately translates to a velocity-dependent mapping between subhalo and stellar mass.

The velocity binned SHMF for M_{inf} and M_{max} (figures 3.6 and 3.7), on the other hand, do show a noticeable difference between the bins. The normalization of the low velocity bin is higher than the high velocity bin. When coupled with the similarity of the SHMFs in $M_{z=0}$, this implies that halos with low velocities have experienced more mass loss than those with higher velocities. Specifically, the normalization in mass of the high velocity bin $M_{z=0}$ SHMF is $\sim 22\,\%$ that of the corresponding M_{max} relation; for the low velocity bin, it is $\sim 17\,\%$. This is exactly what we would expect from lower velocity halos being older, as older halos have lost more mass since their mergers than their younger counterpart.

Furthermore, at the low mass end, the low velocity SHMF turns off from the power law behaviour at a higher mass ($\sim 3 \times 10^{-5} M_{host}$) than the high velocity one ($\sim 2 \times 10^{-5} M_{host}$), suggesting that resolution issues set in at higher masses for those subhalos as well. This is also in keeping with a velocity age gradient: older halos will suffer more severely from artificial relaxation and disruption, since they are part of the main halo for longer.

The actual age distribution of the subhalos in each velocity bin is shown in figure 3.8. There is a distinct difference in the distributions for each velocity bin. The high velocity bin is weighted toward young subhalos, with more than $50\,\%$ merging at $z \lesssim 0.26$ and the number of subhalos declining with increasing redshift. By contrast, more than $40\,\%$ of subhalos in the low velocity bin merge before $z = 0.58$. The middle velocity has a distribution intermediate between the two.

These results all suggest that it should indeed be possible to gain some age information on subhalos from observations of their velocities. There are only a few hundred galaxies with determined spectra in the entire Virgo Cluster, which probe only the highest masses. Spectroscopic redshifts of the galaxies in the Virgo Cluster down to low mass are therefore highly desirable in order to further this research.

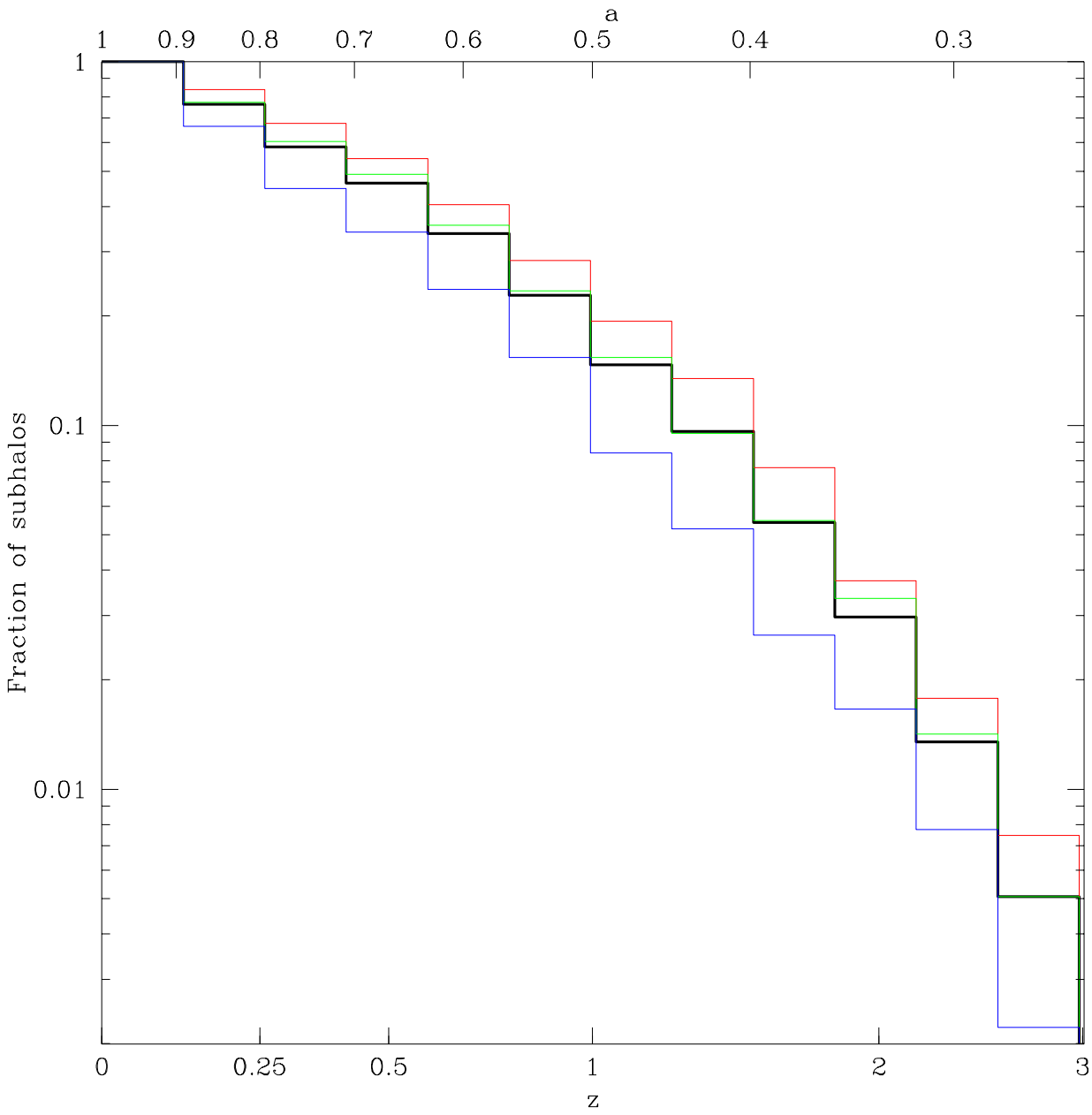

Figure 3.8: Cumulated distribution of subhalo merger times in each velocity bin, expressed as a fraction of all the subhalos in the bin. Colors as figure 3.5. Only halos with $M_{z=0} > 7 \times 10^{-6} M_{host}$ are considered, in order to limit resolution issues.

Chapter 4

Abundance Matching

Having examined the simulations themselves, we now turn to the task of combining them with the observational data.

4.1 Observations: the NGVS

The Next Generation Virgo Survey(Ferrarese et al., 2012) is the next major optical survey of the Virgo cluster, replacing the decades old Virgo Cluster Catalog of Binggeli et al. (1985). When complete, it will cover an area of $\sim 104\,\mathrm{deg}^2$ in the u, g, r, i, and z bands.

Currently, only the central $\sim 4\,\mathrm{deg}^2$ of the NGVS have been completed and analyzed in all five bands.

4.2 The Subhalo Stellar-to-halo Mass Relation

To determine the subhalo SHMR, we use the technique of abundance matching, assuming the most massive satellite galaxy is hosted by the most massive subhalo, the next most massive by the next most massive subhalo, and so on. There are three definitions of the subhalo mass which we can use: $M_{z=0}$, the mass of the subhalo at $z = 0$; M_{inf}, the mass the subhalo had as an independent halo prior to merging into a larger system; and M_{max},

the largest mass the subhalo ever had as an independent halo.

When normalizing the subhalo masses, we take the mass of Virgo as $M_{200,c} = 4.2 \times 10^{14}\,\mathrm{M}_{\odot}$ (McLaughlin, 1999). We convert this to the halo mass definition used by AHF assuming an NFW profile with $c = 2.51$, as adopted by NGVS (Ferrarese et al., 2012), which yields $M_{vir} = 5.76 \times 10^{14}\,\mathrm{M}_{\odot}$.

For our stellar masses, we use the preliminary stellar mass function of the central NGVS region (P. Côté, Private Communication). These data indicate a power law relation down to $10^7\,\mathrm{M}_{\odot}$, below which it deviates due to completeness limits. We therefore use the actual data for $M_{\star}{>}10^7\,\mathrm{M}_{\odot}$; for stellar masses below this, we extrapolate using the power law, which has a slope of -2.38. In practice, only a few of the halos have a sufficient number of subhalos in the central region for the matching to reach the extrapolation mass regime.

Figures 4.1, 4.2, and 4.3 show the SHMR for the three definitions of mass, along with the low redshift fit from L12. There is overall similarity of form between the three SHMRs and the L12 fit, consisting of a power law at low masses transitioning to a steeper relation at higher mass.

4.3 Comparison to Leauthaud et al.

Caution must be used in making direct comparisons between these results and those of L12. Both the halo and stellar masses are derived under different assumptions, leading to different normalizations and positions of the dark-to-stellar mass minimum.

Comparisons at the high mass end are particularly questionable. Firstly, this is the region of greatest variability in the subhalo mass function, as evidenced by the large scatter in the SHMRs. Secondly, this is also the region of greatest variability in the global SHMR. The relation differs for different types of galaxies, and between field and central cluster galaxies. Finally, because we are matching against only one cluster (Virgo), we have only a few galaxies (four with $M_{\star}{>}3 \times 10^{10}\,\mathrm{M}_{\odot}$) to trace the mean stellar mass function.

For these reasons, we will restrict ourselves primarily to considering how the low mass slope, β, of our SHMRs compare to that of the L12 relation. We take the slope from a

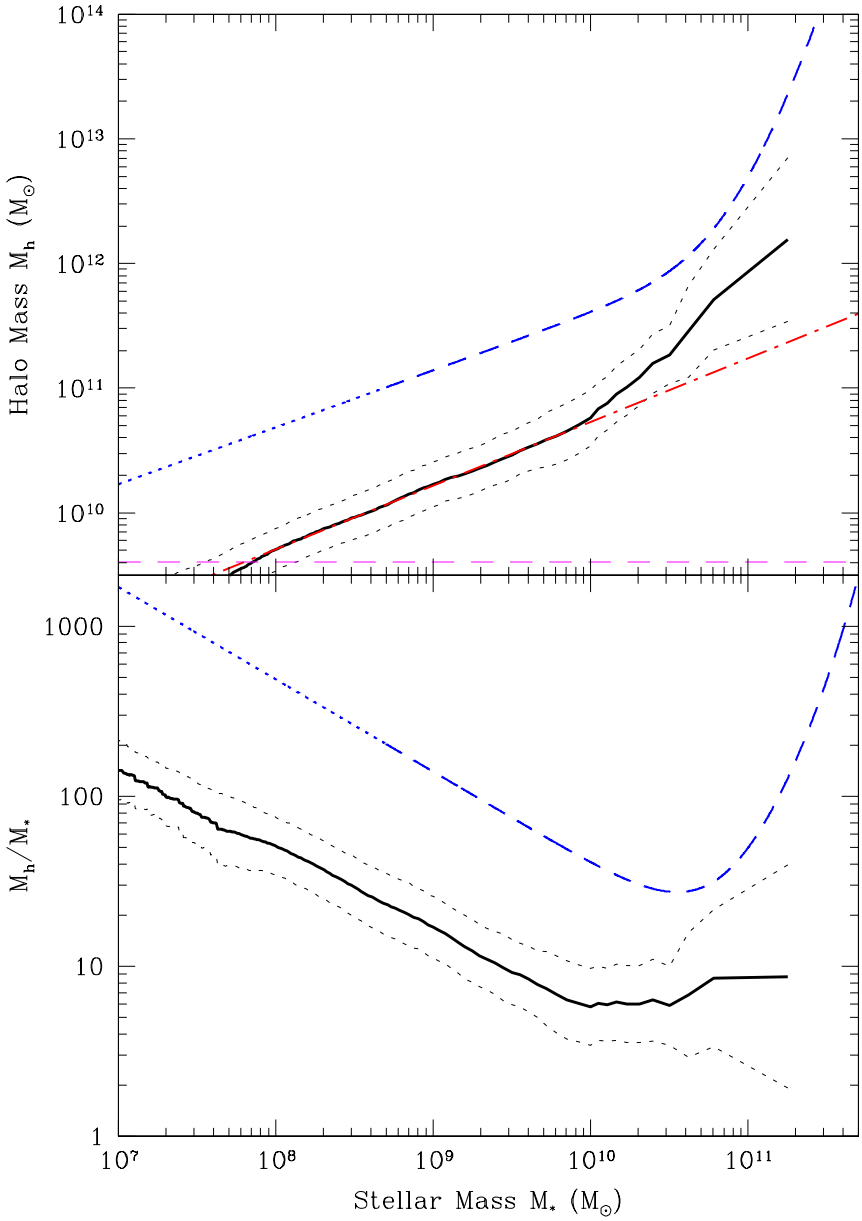

Figure 4.1: Top panel: the stellar-halo mass relation from abundance matching using the final mass $M_{z=0}$. The solid black line is the mean SHMR, defined here as $\langle \log (M_h (M_\star)) \rangle$; the dotted lines are the 1σ variation about this mean. The dashed blue line is the $z = 0.37$ result from L12; dotted is the extrapolation to lower masses. The horizontal dashed line is the $7 \times 10^{-6} M_{host}$ resolution limit. Between $M_\star = 10^8$ and $10^{10}\,\mathrm{M}_\odot$, the SHMR is well fit by a power law of index 0.51 (red dot-dashed line). Lower panel: the dark-to-stellar mass ratio for the same versus stellar mass.

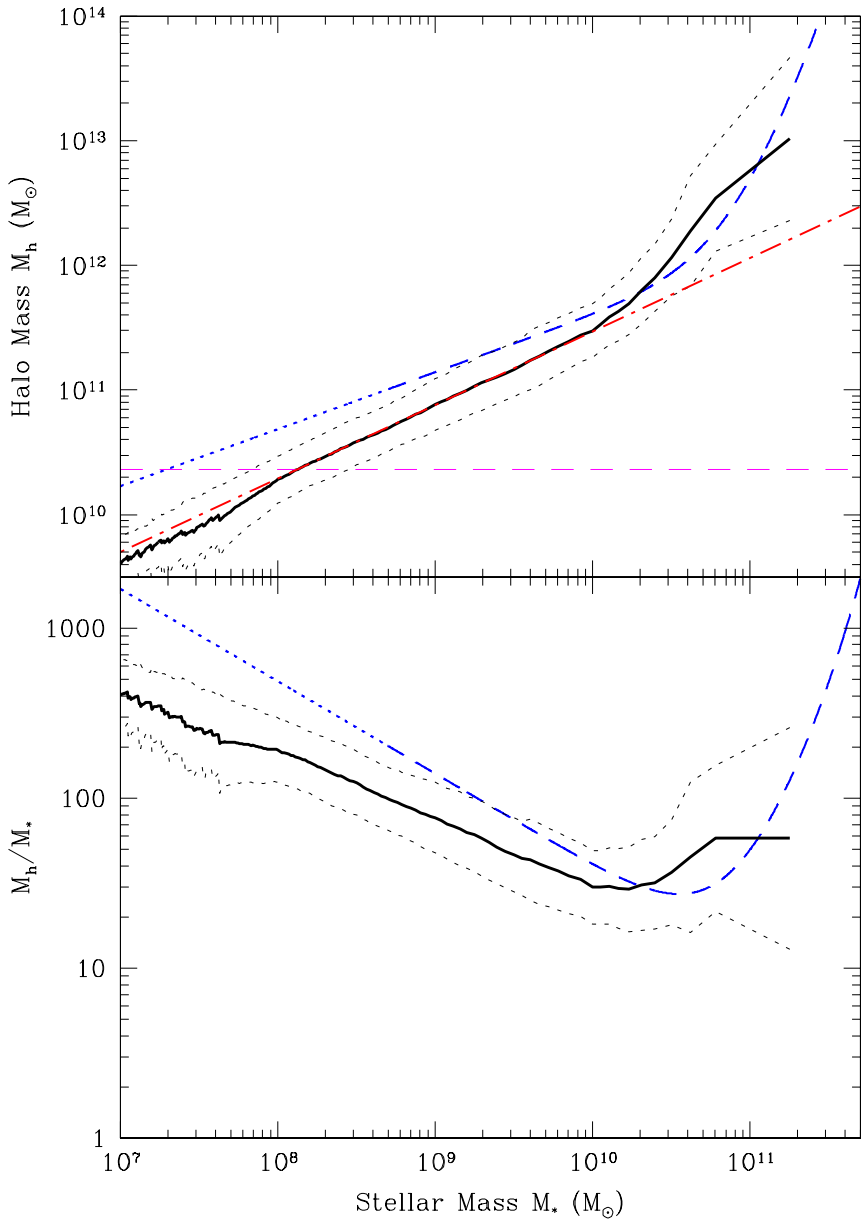

Figure 4.2: As figure 4.1, but from abundance matching using the infall mass M_{inf}. The power law fit between $M_\star = 10^8$ and $10^{10}\,\mathrm{M}_\odot$ has index 0.59. The horizontal dashed line is the $4 \times 10^{-5} M_{host}$ resolution limit.

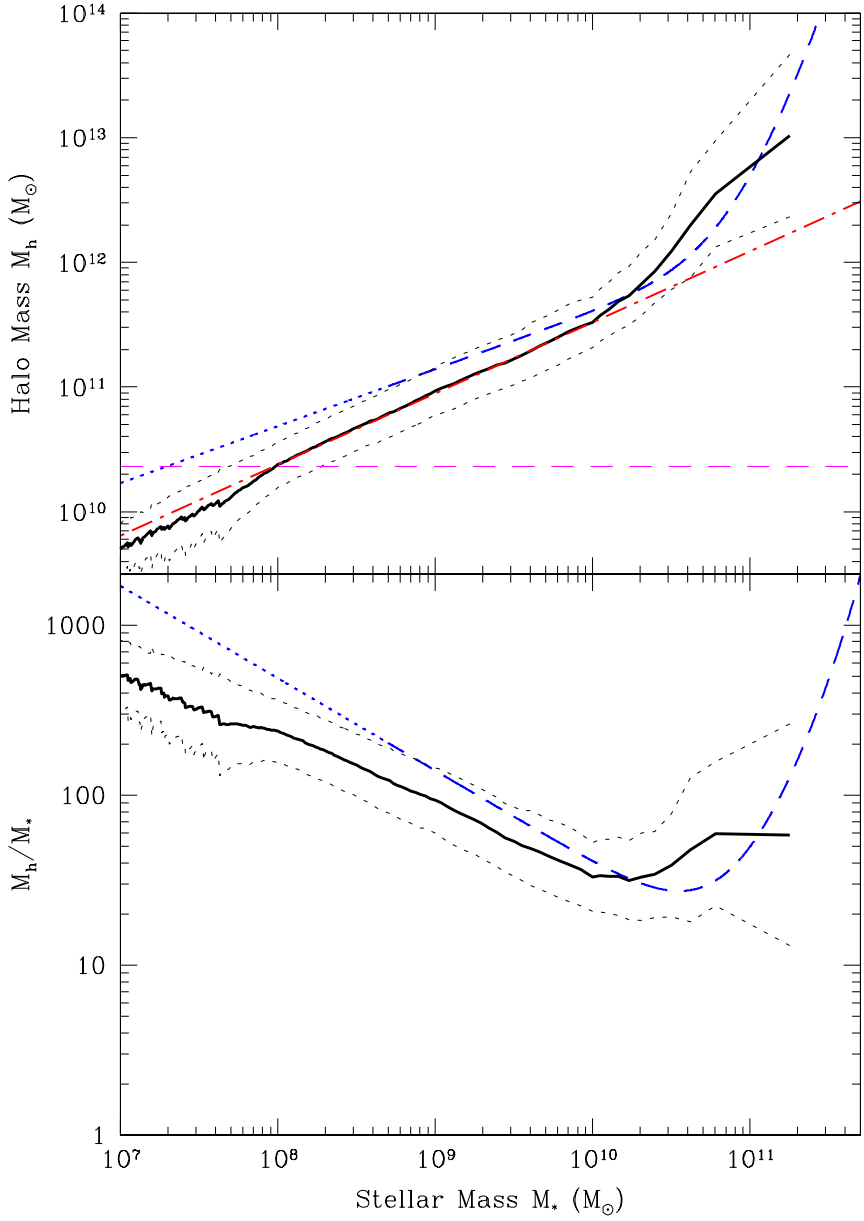

Figure 4.3: As figure 4.1, but from abundance matching using the maximum mass M_{max}. The power law fit between $M_\star = 10^8$ and $10^{10}\,\mathrm{M}_\odot$ has index 0.57. The horizontal dashed line is the $4 \times 10^{-5} M_{host}$ resolution limit.

linear fit to the mean relation between $M_\star = 10^8$–$10^{10}\,\mathrm{M}_\odot$, which excludes the regions of the high mass turn up and the low mass resolution limit. We estimate the error from the scatter in slopes obtained by fitting each individual SHMR separately.

The most distinctive feature of the $M_{z=0}$ SHMR (figure 4.1) is its much lower normalization. This is entirely expected. After merging with the main halo, the outer material of the subhalos are stripped away, reducing its mass to a fraction of its original mass, while the much more compact galaxies at their centers remain intact. In the absence of any other effect, at a fixed stellar mass satellite galaxies in clusters will have smaller host (sub-)halos than their field counterparts. Part of the normalization difference may come from the different mass derivations; but most of it will be real.

Beyond this, however, there is the difference in the low mass slope β. For our $M_{z=0}$ SHMR, we find $\beta_{z=0} = 0.50 \pm 0.02$, in contrast to L12, who found $\beta = 0.46$. While only a 0.04 difference, L12 also found that the slope was remarkably constant out to $z = 0.88$.

Both the M_{inf} and M_{max} SHMRs (figures 4.2 and 4.3) are similar, as implied by the similarity of the equivalent subhalo mass functions (see section 3.2). For both, β is markedly steeper ($\beta_{inf} = 0.60 \pm 0.02$, $\beta_{max} = 0.56 \pm 0.02$) than the L12 relation. The normalization is once more lower than L12, though this can partly be explained through the different mass definitions.

The abundance matching technique is of course a simplification; in reality, there will be scatter in the masses, and ranks in stellar and halo mass will not exactly correspond. To judge the effect of scatter on the slope, we take the subhalos of each data set and scatter the ranks by a factor of two, i.e. for each subhalo the new rank R' is defined through $\log(R') = \log(R) + \delta$, where δ is randomly and taken uniformly from the interval $[-\log(2), \log(2)]$. We then sort by these new ranks, and perform the abundance matching again. This test reveals that the effect of scatter is to make the low mass slope steeper rather than shallower, so scatter cannot be used to explain the difference with the global SHMR.

Regardless of what mass is used to define it, it is clear that the SHMR for subhalos is distinctly different from that of halos in the field. Any attempt construct the global SHMR must therefore take this into account.

4.3.1 A Test of Consistency

The comparison of our results to L12 is limited by the fact that we are measuring different things: namely the SHMR of subhalos and of halos; subhalos are older than halos in the field. To check if our results are consistent with L12, we consider a simple model, in which the SHMR does not change in shape, but merely shifts in stellar mass with redshift, i.e.

$$M_\star\left(M_h, z\right) = M_\star\left(M_h\right) g\left(z\right).$$

Assigning a stellar mass to each subhalo based on M_{inf} or M_{max} and the infall redshift z_m, we obtain a relation which can be compared to our SHMRs. Since L12 found a near-constant β and the evolution in shape primarily occurs in the high mass regime, where there are the fewest subhalos, this toy model should produce reasonable results in the low mass regime.

For the shape of the relationship, we use the L12 $z = 0.37$ result, and select $g\left(z\right)$ such that model matches this at $z = 0.37$. Testing various simple functions for $g\left(z\right)$, a clear trend emerges.

If the function $g\left(z\right)$ used is such that the dark-to-stellar mass ratio is higher at fixed halo mass at low redshift than at high redshift, and thus hosted smaller galaxies in the past, then the slope of the resultant relationship is steeper than the original model, like we find with our SHMRs compared to L12.

Conversely, if the opposite holds true, and $g\left(z\right)$ is such that the dark-to-stellar mass ratio increases at high redshift for fixed halo mass, and such halos were host to more massive galaxies in the past, then the slope of the resultant relation is shallower, which is not what we observe.

Figures 4.4 and 4.4 show two specific examples, using M_{inf} and $g\left(z\right) \propto \left(1+z\right)^\alpha$, for $\alpha = -3$ and 3, respectively (other α, functional forms, and using M_{max} instead all produce similar results.) $\alpha = -3$ qualitatively reproduces the steeper slope of our SHMR relative to the L12 result, while $\alpha = 3$ causes the opposite trend.

While the model does not reproduce steepness of the high mass ($M_\star \gtrsim 10^{10.25}\,\mathrm{M}_\odot$) slope, it should not be expected to. The high mass region is where most of the evolution

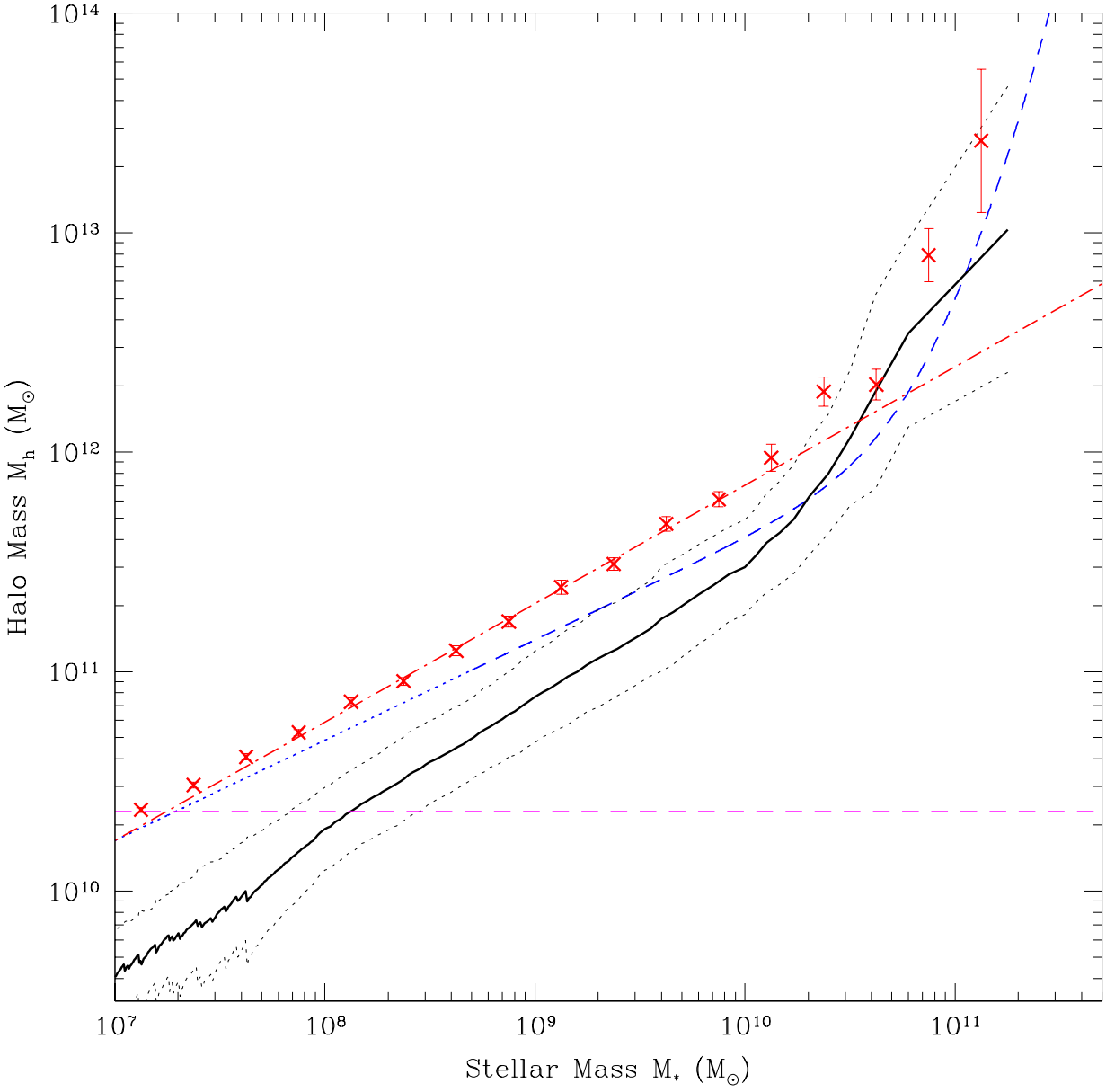

Figure 4.4: The toy model compared to the SHMR, using M_{inf} and $g(z) \propto (1+z)^{-3}$. Plot follows the top panel of figure 4.2. The red points are the observed relation that results from the toy model. Red dot-dashed line is a power law fit between $M_\star = 10^8$ and $10^{10}\,\mathrm{M}_\odot$ of index 0.54.

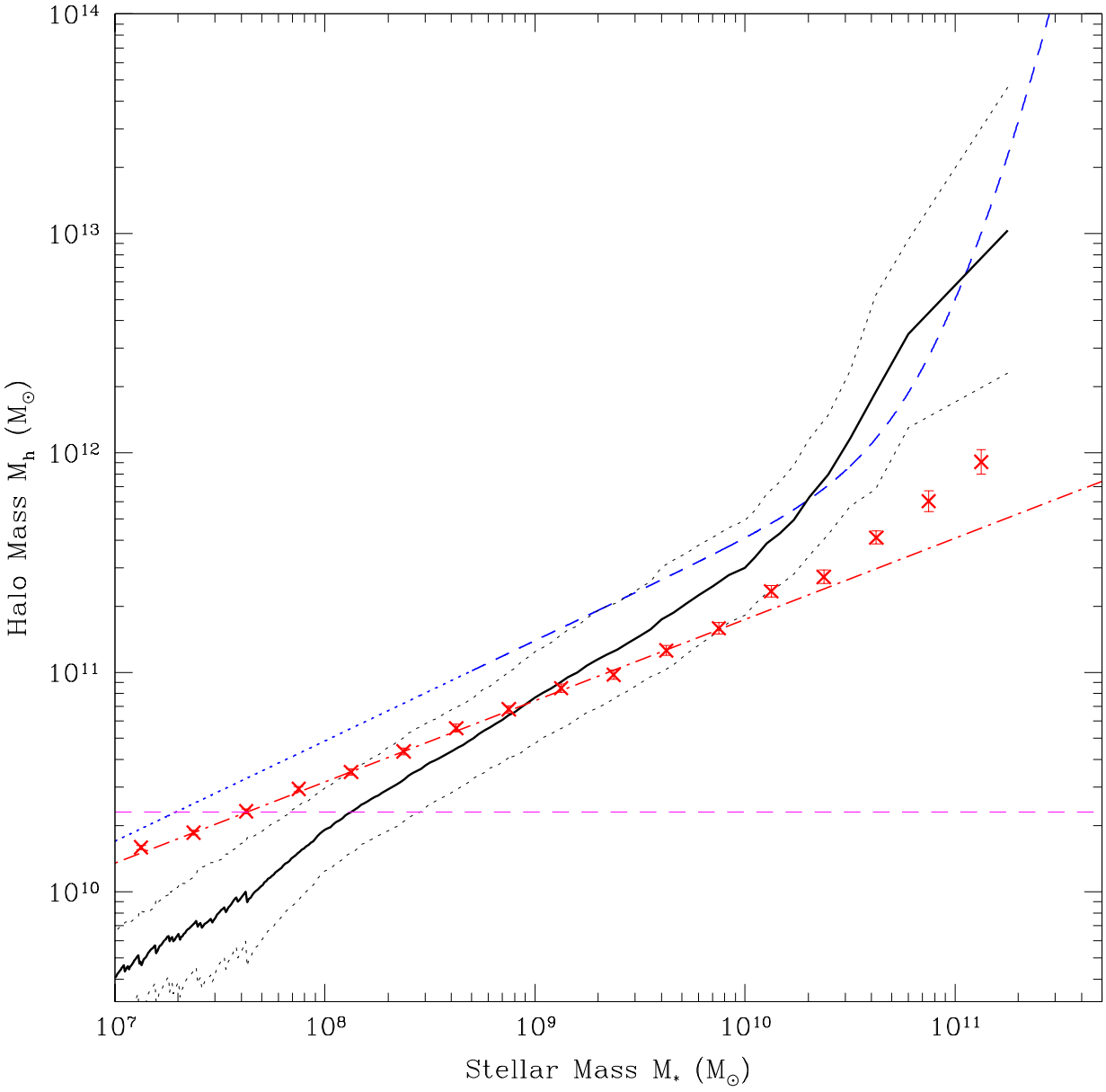

Figure 4.5: As figure 4.4, using $g(z) \propto (1+z)^3$. The power law has index 0.37.

in the L12 SHMR occurs, which is not accounted for in the model.

Overall, the normalization of the model result is rather higher than the SHMR. This is not a great concern, as the toy model has several deficiencies which can account for much of the difference. Firstly, the normalization of the model relation is based on different stellar and halo masses than those we apply it to. It also assumes that star formation ceases as soon as a halo merges into the main halo, which is probably not the case.

These tests imply that our results are qualitatively consistent with L12 as long as the dark-to-stellar mass ratio decreases with time. This is in keeping with the conclusions of L12, whose preferred model for the evolution of the SHMR requires that the normalization (and thus the dark-to-stellar ratio) of the low mass relation decreases with time, and the results of Behroozi et al. (2010), who find just such an evolution from $z = 1$ to $z = 0$.

The conclusion from this toy model, however, contradicts the expectations of another simple test. Smaller subhalos tend to be older, and larger ones younger (Taylor & Babul, 2005). With a steeper low mass slope, the subhalo SHMR is further below the L12 relation at the lowest stellar masses than it is at higher mass; or, equivalently, the galaxies in older subhalos have lower dark-to-stellar mass ratios, relative to that of objects of the same mass at low redshift, than younger galaxies relative to their equivalents. Under the assumption of a constant low mass slope, this implies that our subhalo SHMRs indicate a decrease in the normalization of the low mass SHMR (and the dark-to-stellar mass ratio) at higher redshift—exactly the opposite conclusion of the toy model and Behroozi et al. (2010).

It is not entirely clear exactly why these two tests give contradictory results. Resolution may be more of an issue than our tests of chapter 3 indicate. Further modelling will be required to definitively resolve this discrepancy.

Chapter 5

Mergers and Mixing

Halos are not static structures, but grow in mass. Part of this growth comes from the diffuse matter surrounding the halo collapsing on to it and virializing. We would expect this new material to be added on the outside of the halo, smoothly increasing the virial radius and mass as the halo grows. The result is a radial age gradient, with the material having been part of the halo longer the closer it is to the center.

Mergers change this picture. Much like throwing a rock into a pond, an incoming halo can disturb the age gradient, mixing old and new material as it passes though and merges with the main halo. In principal, this can have any effect from smearing the gradient out a little to destroying it completely to even inverting it, if the merger were to kick the central material out into the outskirts.

It is already known that mergers change the structure of a halo, through the concentration c (see e.g. Zhao et al. (2003)). During slow growth, c increases, as material is added to the outside of the halo, increasing r_{vir} without affecting the profile (r_s). During periods of rapid growth (i.e. large mergers), however, c remains constant or decreases, which means that r_s is increasing at least as fast as r_{vir}, and thus that the center of the halo is being disturbed by the mergers. It seems probable that such disturbance would be accompanied by the mixing of old and new material.

Given a merger between a pair of halos, the larger primary halo and the smaller secondary, we might ask how the amount of mixing in the primary depends on the ratio between their masses, M_{pri}/M_{sec}. One would naturally expect major mergers, where the

secondary halo is closer in mass to the primary, to cause more mixing than minor mergers, the difference between tossing in a boulder or a pebble.

5.1 The Simulation and the Merger Catalog

To investigate the mixing that occurs during mergers, we need a large number of suitable mergers from a simulation. They are taken from a 512^3 particle simulation of a $120\,h^{-1}$Mpc side box. The cosmology of the simulation is based on WMAP7 ($\Omega_b = 0.0456$, $\Omega_c = 0.227$, $\Omega_\Lambda = 0.7274$, $H_0 = 70.4\,\mathrm{km\,s^{-1}\,Mpc}$, $n = 0.963$, $\sigma_8 = 0.809$). The halos are found with the FOF code, and connected into merger trees with our tree code.

From the simulation and the merger trees, we construct a catalog of mergers meeting the following constraints:

Primary size Only mergers in which the primary (larger) halo has at least 300 particles are included, so that there are a substantial number particles used to calculate the mixing.

Merger Ratio We restrict ourselves to mergers with a ratio of 10:1 or less.

Clean Primary For a merger to be included in the catalog, the primary halo must not have recently undergone a significant merger. Such a halo will still be under the influence of the previous merger, and it is not possible to separate the effects of each merger from one another. For this purpose, we require that in the previous 0.2 the age of the universe, the mass of the primary halo does not change between successive snapshots by more than 5 % (i.e. that it does not undergo a merger of ratio 20:1 or less).

Post Merger Interference Similarly, if another merger occurs shortly after the merger of interest, the effects of the two mergers will not be distinguishable. We thus require that the mass of the halo resulting from the merger does not change between successive snapshots by more than 5 % before the snapshot we use for the final state.

With these constraints, our catalog contains 908 mergers.

5.2 Measuring Mixing

For each merger in the catalog, we use two snapshots to evaluate the amount of mixing. The initial state of the system is taken from the snapshot immediately prior to the merger, while the final state is taken from the first clean snapshot at least 0.50 times the age of the universe at the time of merger. A clean snapshot is one in which the descendant halo is not lumped by the FOF algorithm with other interfering halos, defined as when the halo of interest comprises at least 91 % of the particles in the FOF halo.

The interval of 0.50 the age of the universe is chosen to ensure that the mixing has a chance to take place. The radial orbital period of a subhalo is approximately equal to the age of the universe at the time of merger, with the pericentric passage occurring between 0.125 and 0.25 of a period, depending on the eccentricity, after it first crosses the virial radius (Taylor & Babul, 2004). By using the factor of 0.50, the secondary halo will have gone through one pericentric passage and will have returned to the outskirts of the primary at the time mixing is evaluated.

We measure the amount of mixing that occurs during a merger with Spearman's rank correlation coefficient. The Spearman coefficient is a measure of the strength of the dependence between two variables through a monotonic function. Rather than operating on the values of the variables themselves, it instead operates on the rankings of the values.

The Spearman coefficient is defined as

$$\rho = \frac{\sum_i (x_i - \bar{x})(y_i - \bar{y})}{\sqrt{\sum_i (x_i - \bar{x})^2 \sum_i (y_i - \bar{y})^2}},$$

where x and y are the rankings of the variables. The value of this quantity ranges from -1 to 1. A value of 1 indicates the variables are perfectly related by an increasing monotonic function, while a value of -1 indicates a decreasing monotonic function. A value of 0 indicates no correlation between the variables. Notably, the exact form of the function relating the variables is irrelevant: any function, so long as it is monotonic, will show perfect (anti-)correlation through the Spearman coefficient.

5.2.1 Radial Mixing

To measure the amount of radial mixing in a merger, we calculate the Spearman coefficient on the radii, measured from the location of the most bound particles, of the particles before and after the merger. The Spearman coefficient has the benefit of being insensitive to simple geometric changes. If a halo is merely heated by a merger, such that the whole halo expands without the radial order of the particles changing, the Spearman coefficient will show no mixing.

There are three possibilities, depending on the value of the Spearman coefficient:

a) $\rho \sim 1$. The merger barely affects the halo, leaving the distribution of the material within it mostly unchanged.

b) $\rho \sim -1$. The merger inverts the halo, the material at the center being thrown out to the outskirts.

c) $\rho \sim 0$. The merger completely randomizes the particles of the halo. Where a particle is before the merger has no predictive power as to where it is after the merger.

We measure the mixing in four bins of equal width in $\log(M_{pri}/M_{sec})$, so that the upper two consist of major mergers and the lower of minor mergers.

Figure 5.1 shows the results of measuring mixing through radius. The data tend to be concentrated around $\rho \sim 0.65$, indicating only a moderate amount of mixing. There is a large amount of scatter, particularly in the last (most major) bin. It is possible that some of this is due to outliers, resulting from imperfectly excluding mergers with confounding effects, but in the main it looks to be real.

There is a trend towards more mixing occurring in more equal-mass mergers, $\bar{\rho}$ decreasing from 0.62 to 0.53 from the highest to lowest ratio bins. However, this difference is small compared to the amount of scatter in each bin.

It is interesting to note the reasonably well-defined upper limit to the distribution at $\rho \sim 0.75$. Combined with the small amount of evolution, one might cautiously postulate that this represents a lower bound to the amount of radial mixing that will occur even in the absence of mergers. If this is the case, then even major mergers are capable of leaving the radial age gradient undisturbed beyond the background level: highly surprising, given

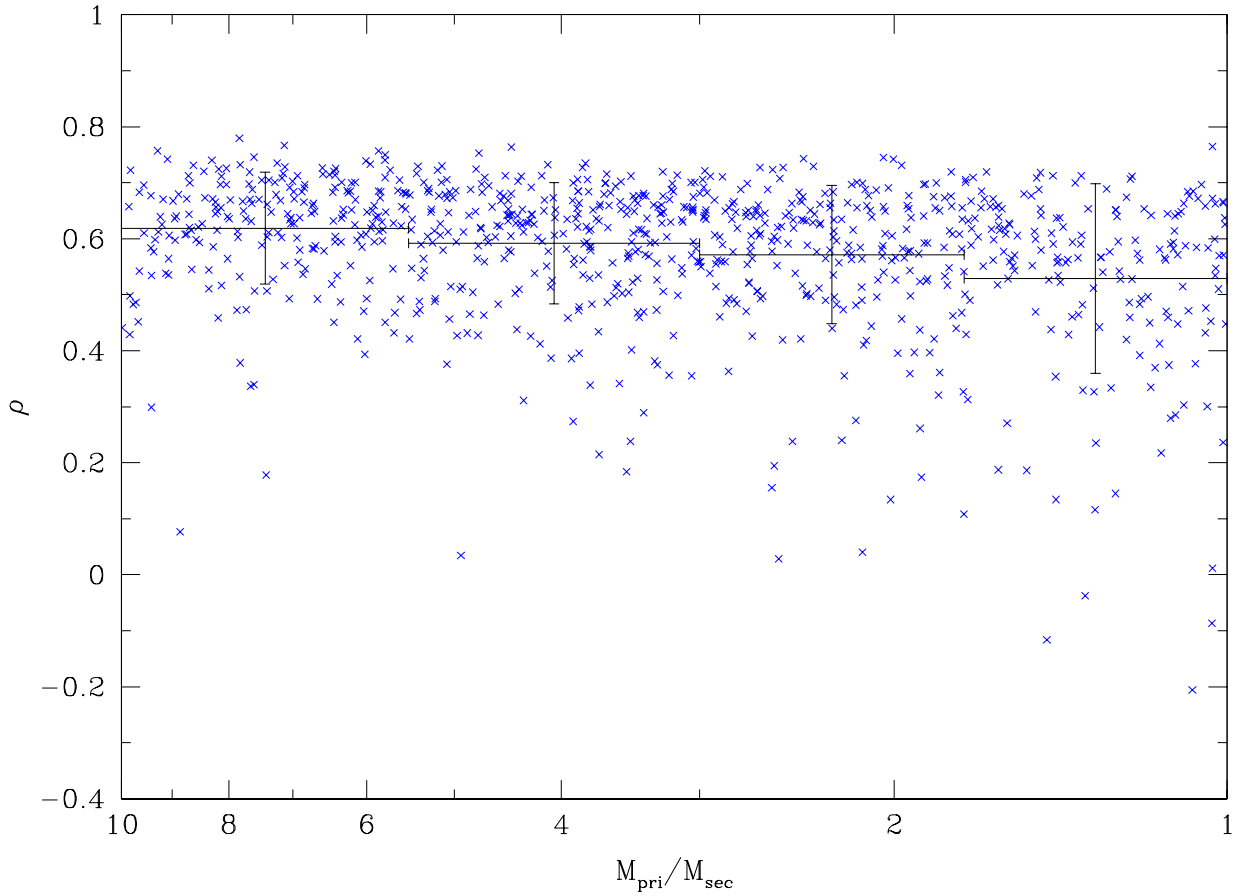

Figure 5.1: Spearman's rank correlation coefficient in radius versus merger ratio, with the mean in each bin. The horizontal error bars show the width of the bins. Vertical error bars are the 1σ variation within the bin.

the large addition of energy and angular momentum such a merger represents.

Overall, it appears that, while the merger ratio does have an effect on the amount of mixing, there are other factors which have greater effect. In light of the expectation that major mergers should cause large amounts of mixing, this suggests that perhaps radius is not the best measure to use to describe mixing, and another measure should be tried.

5.3 Mixing in Energy

The orbits of particles in a halo tend to be highly radial. Even in the complete absence of particle interaction, e.g. with massless particles in a static background potential, the Spearman coefficient will indicate some radial mixing as the particles moved along their orbits and change their ordering.

Instead of radial mixing, we can measure mixing in the total energy (kinetic + potential) of the particles. This quantity provides an alternate definition for the centralness of the particles, with the "innermost" particles having the most negative energies. Unlike radius, however, it will, in the absence of other effects, remain constant for a particle as it travels along its orbit. Interactions with other particles will of course cause deviation from the ideal behaviour; nevertheless, the energy lacks the inherent mixing signal found in radius.

Since a merger adds mass to a halo, it inherently changes the energies of the particles by increasing the depth of the potential well, regardless of any other effect. However, this change in potential affects all particles in the same way, leaving the order of the energies unchanged. The Spearman coefficient is thus insensitive to this effect.

The total energy of the particles are calculated from the velocities and potentials provided in the Gadget2 snapshot.

Figure 5.2 shows the results of measuring mixing through energy. The trend of increased mixing with decreasing merger ratio is once again present. There is much less scatter than when measured through radius, and the scatter being more similar across the

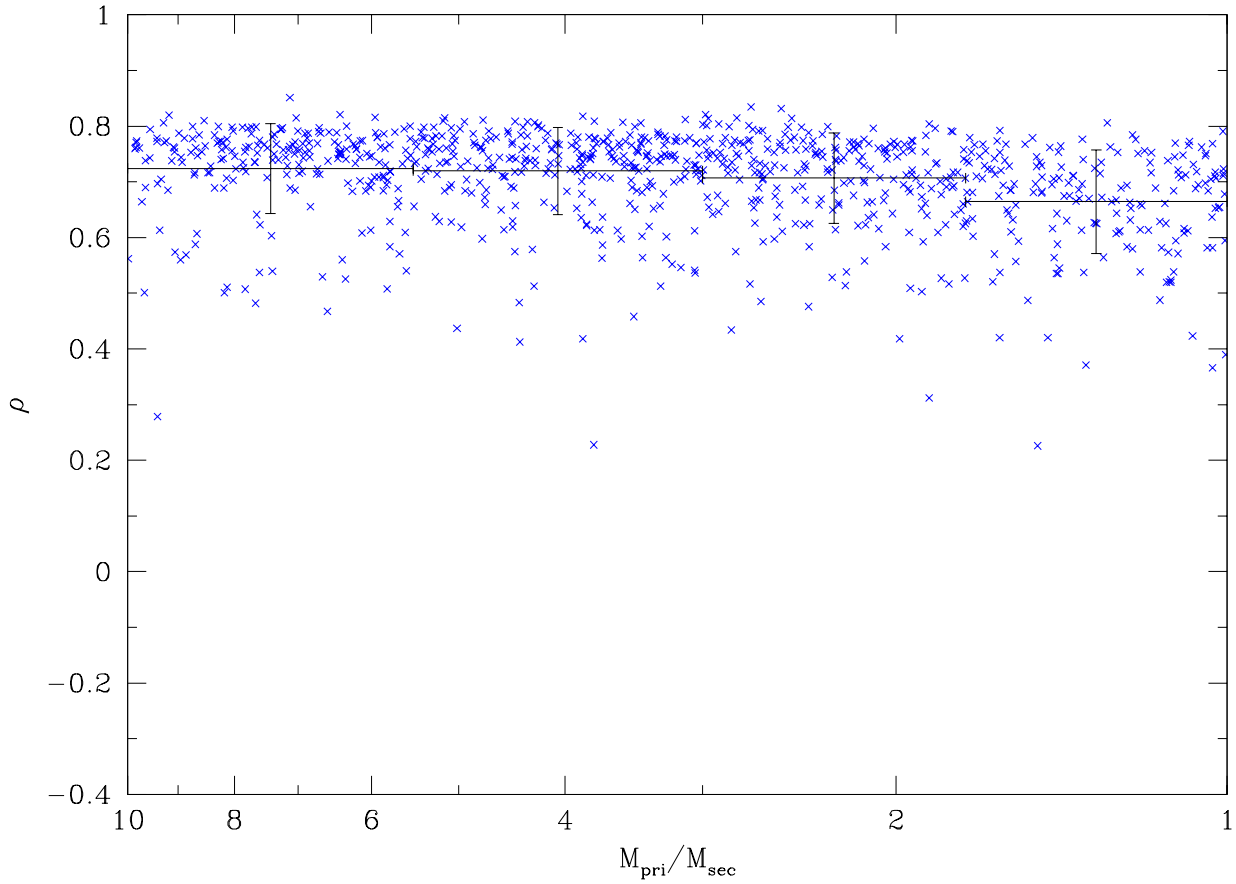

Figure 5.2: As figure 5.1, but with Spearman's rank correlation coefficient in energy.

bins, with the lowest ratio bin once again having the largest scatter. The data in general tends to higher ρ, not unexpected given the greater stability of the energy as outlined above.

The difference is however, smaller than that found for radius. The Spearman coefficient only decreases from 0.72 to 0.66 between the highest and lowest ratio bins, counteracting the smaller scatter.

Once again there is a fairly sharp upper limit to ρ, only a handful of mergers having ρ>0.82. Taking this as the minimum mixing in energy, we find again that, while major mergers do tend to cause more mixing, they are also able to leave the halo unmixed relative

to the background.

We find then that when mixing is measured through energy, merger ratio continues to be only a minor factor in the amount of mixing that occurs.

5.3.1 Results

Contrary to expectation, neither mixing in energy nor radius show a clear effect of major mergers being major mixers. The data suggest that, while major mergers may cause significant amounts of mixing, they can just as easily cause none relative to the background level, despite the large disruption they represent.

The mixing effect of mergers is probably more subtle and complicated then we initially concluded, and cannot be accurately captured in the coarse measure of the Spearman coefficient over the whole halo. Further work is required to understand what happens to the age distribution of material during mergers.

Chapter 6

Conclusions

The Virgo cluster is the nearest galaxy cluster, and as such provides a unique testing ground for the predictions of the ΛCDM model. The Next Generation Virgo Survey is extending observations of its member galaxies down to unprecedented low stellar masses, in exactly that regime where ΛCDM is most in need of verification.

Using high-resolution simulations of Virgo-like clusters, the preliminary results of NGVS, and the technique of abundance matching, we can begin to investigate the relation between the masses of satellite galaxies and their host subhalos.

We find that the stellar-to-halo mass relation for subhalos is distinctly different than the global relation for halos in the field found in L12. This is true regardless of how the subhalo mass is defined. This has implications for models such as that of Behroozi et al. (2010), where the global SHMR is assumed to also apply to subhalos, with the mass defined as the mass at the time of merger.

Since our data cover only the central region of the Virgo cluster, it is possible that the differing SHMR arises from this limitation. An analysis of the cluster as a whole may reveal a cluster-wide SHMR more in line with the global relation. Even if this is so, however, it merely opens another avenue of research, as such a result would mean that the subhalo SHMR is dependent upon position within the cluster. We must wait for the full results of the NGVS survey before such possibilities can be investigated.

Our results are inconclusive as to whether our SHMRs are consistent with the global SHMR results of L12, taking into account the evolution of the subhalos after infall. We construct a toy model which is capable of qualitatively reproducing our results as long at the dark-to-stellar ratio normalization of the low mass relation increases with increasing redshift. However, this is contradicted by a simple test based on the average ages of subhalos of different mass, which indicates that the opposite must be true: the normalization of the dark-to-stellar ratio decreases with increasing redshift. Further modelling is necessary to clear up this confusion.

Any attempt to extract redshift-dependent trends from the properties of the satellite galaxies and subhalos requires finding a relation between some of those properties and the merger redshift, particularly velocity and radius.

From our simulations, we find that there is an age gradient in the velocity of subhalos: subhalos with greater line-of-sight velocities relative to the main halo tend to be younger than those with smaller velocities. Furthermore, the gradient is distinct enough to cause significant differences in the mean relations between the infall and final subhalo masses. This suggests that velocities can provide useful information about the histories of subhalos and reveal merger-redshift dependent trends in the relation between subhalos and their hosted galaxies. Well-determined spectroscopic redshifts of the galaxies of the Virgo cluster down to low masses may therefore be a valuable resource to complement the NGVS survey and unravel the mysteries of galaxy evolution in a cluster environment.

A radial age gradient should naturally arise from the slow accretion of material, so that younger subhalos exist at larger radii. Major mergers, being disruptive events, have the potential to disturb this gradient. In order to make use of the potential relation between radius and age, we must be able to character the extent to which mergers destroy it.

Naively, one would expect that major mergers, representing a larger disruption to the equilibrium of the halo, would cause more mixing than less disruptive minor mergers. Although we do find evidence for this effect when measuring mixing both in radius and in energy, we find that it is small compared to the amount of scatter, and that the amount of mixing that occurs during a merger is usually not large, regardless of the merger ratio.

References

Behroozi, P. S., Conroy, C., & Wechsler, R. H. 2010, ApJ, 717, 379

Behroozi, P. S., Wechsler, R. H., & Conroy, C. 2012, ArXiv e-prints

Binggeli, B., Sandage, A., & Tammann, G. A. 1985, AJ, 90, 1681

Blanton, M. R., Geha, M., & West, A. A. 2008, ApJ, 682, 861

Ferrarese, L., Côté, P., Cuillandre, J.-C., et al. 2012, ApJS, 200, 4

Fraternali, F., van Moorsel, G., Sancisi, R., & Oosterloo, T. 2002, AJ, 123, 3124

Gunn, J. E., & Gott, III, J. R. 1972, ApJ, 176, 1

Hansen, S. M., Sheldon, E. S., Wechsler, R. H., & Koester, B. P. 2009, ApJ, 699, 1333

Klypin, A., Kravtsov, A. V., Valenzuela, O., & Prada, F. 1999, ApJ, 522, 82

Knollmann, S. R., & Knebe, A. 2009, ApJS, 182, 608

Komatsu, E., Smith, K. M., Dunkley, J., et al. 2011, ApJS, 192, 18

Leauthaud, A., Tinker, J., Bundy, K., et al. 2012, ApJ, 744, 159

McLaughlin, D. E. 1999, ApJ, 512, L9

Mei, S., Blakeslee, J. P., Côté, P., et al. 2007, ApJ, 655, 144

Moore, B., Ghigna, S., Governato, F., et al. 1999, ApJ, 524, L19

More, S., van den Bosch, F. C., Cacciato, M., et al. 2011, MNRAS, 410, 210

Moster, B. P., Somerville, R. S., Maulbetsch, C., et al. 2010, ApJ, 710, 903

Navarro, J. F., Frenk, C. S., & White, S. D. M. 1997, ApJ, 490, 493

Peng, Y.-j., Lilly, S. J., Kovač, K., et al. 2010, ApJ, 721, 193

Power, C., Navarro, J. F., Jenkins, A., et al. 2003, MNRAS, 338, 14

Press, W. H., & Schechter, P. 1974, ApJ, 187, 425

Ryden, B. 2003, Introduction to cosmology

Sheth, R. K., Mo, H. J., & Tormen, G. 2001, MNRAS, 323, 1

Springel, V. 2005, MNRAS, 364, 1105

Taylor, J. E. 2011, Advances in Astronomy, 2011

Taylor, J. E., & Babul, A. 2004, MNRAS, 348, 811

—. 2005, MNRAS, 364, 515

Taylor, J. E., & Navarro, J. F. 2001, ApJ, 563, 483

Urban, O., Werner, N., Simionescu, A., Allen, S. W., & Böhringer, H. 2011, MNRAS, 414, 2101

van den Bosch, F. C., & Swaters, R. A. 2001, MNRAS, 325, 1017

Wong, A. W. C., & Taylor, J. E. 2012, ApJ, 757, 102

Zhao, D. H., Mo, H. J., Jing, Y. P., & Börner, G. 2003, MNRAS, 339, 12